NTNU – Trondheim
Norwegian University of
Science and Technology

Nano- porous proppants for shale oil and gas production

Eirik Ottestad

Materials Science and Engineering
Submission date: July 2014
Supervisor: Tor Grande, IMTE

Norwegian University of Science and Technology
Department of Materials Science and Engineering

Oppgavetekst

I de siste årene har det vært en betydelig utvikling i produksjon av olje og gass fra skifer, hovedsakelig i USA. Økt tilførsel har resultert i en nedgang i gassprisen i Nord-Amerika og spådommer om at USA vil være selvforsynt med olje i framtiden. Denne utviklingen har vært akselerert på grunn av store framskritt innen to teknologiområder: horisontal boring og «oppsprekking» av reservoaret. Under oppsprekking av reservoaret ved hjelp av vann under høyt trykk blir såkalte «proppant» tilsatt til reservoaret. En proppant er en sterk partikkel vanligvis av α-alumina (Al_2O_3) som bidrar til å holde disse sprekkene åpen.

Nå er vi interessert i å utvikle proppanter med en porøs struktur, men likevel med tilstrekkelig styrke. Med en porøst proppant har vi muligheten til å innføre en reaktant eller katalysator direkte inn i reservoaret under oppsprekking for *in situ* oppgradering av hydrokarbonene i reservoaret. I et tidligere prosjekt ved instituttet har vi identifisert noen kandidatmaterialer, for eksempel $MgAl_2O_4$ spineller kalsinert ved høye temperaturer. Et elektronmikroskopibilde og fordeling av et Ni i en slik porøs partikkel som inneholder $NiAl_2O_4$ av er vist under. Oppgaven vil omfatte syntesen av kandidatmaterialer, røntgendiffraksjon for å følge faseomvandlinger og reaksjoner etter varmebehandling. Mekaniske egenskaper avgjøres med måling av Vicker's hardhet der en metode er utviklet ved instituttet.

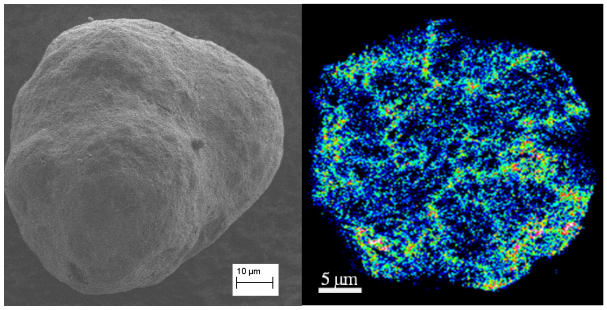

Preface

The present master thesis is based on work carried out at the department of Materials Science and Engineering at the Norwegian University of Science and Technology (NTNU). Work is in cooperation with Statoil, Rotvoll. Reported results are obtained in laboratories at NTNU in Trondheim fall semester 2013 and spring semester 2014.

Firstly, I would like to express my gratitude towards my main supervisor, Professor Tor Grande for excellent and effective guidance, valuable learning's, and both motivational and constructive feedback during this work. I also like to acknowledge my co- supervisors Professor Erling Rytter, Sigrid Eri and Torild Hulsund Skagseth for taking a part of this work, for laboratory guidance and for provideing such an interesting subject to work with. I would like to thank Jens Vindstad for involvement, and useful feedback on presentations.

I like to thank Professor Kjell Wiik for very useful tips, comments and directions, Susanne Linn Skjærvø for help with various questions and much appreciated feedback on presentations, and also Assoc. Prof. Fride Vullum-Bruer together with all members of the "ceramics- group" for positive attitude, helpful advice and feedback. The technical staff of the department must also be acknowledged, especially Julian R Tolchard, Gunn Torill Wikdahl and Elin Harboe Albertsen for providing training, technical support and equipment. I also like to acknowledge Xinzhi Chen help with various practical challenges.

Abstract

Over the last decade a rapid increase in utilization of unconventional reservoirs ha occurred due to advances in horizontal drilling and multi-stage fracturing technology. Reservoirs that earlier were far beyond commercial reach are today producing oil and gas in competitive manner. The share of energy provided form unconventional reservoirs is projected to keep growing relative to conventional energy sources in the years to come. Proppants are essential component in hydraulic fracturing operation as they are placed in fractures and offers increased permeability for the relative impermeable rock- formations present in unconventional reservoirs. Production efficiency may be improved by altering proppants in terms of: mechanical, physical, reactive, and geometrical properties.

Development of strong nano- porous material for proppant applications opens the possibility of multi- functional proppant- solutions. A proppant material with high surface area applied in high temperature reservoirs may enable catalytic reactions on proppant surfaces and thereby in- situ upgrade hydrocarbons. Proppant with high degree of open porosity can enable proppants to be impregnated with surfactants that reduces friction between proppants and oil migrateing through the interstitial void space between particles during operation. Because of high closure- stress occurring in fractures, the most important proppant-material property is high mechanical strength.

Experimental objectives were to adjust synthesis parameters and modification methods to achieve best possible combination of tensile strength, open porosity and high surface- area. Nano- porous γ-alumina spheres modified by impregnation of a magnesium oxide precursor and subsequent calcinations is under current investigation. Impregnations of alumina spheres were carried out using two different methods. Traditional incipient wetness impregnation was carried out in addition to more experimental approach using ultrasonic waves to aid impregnation.

Results show that α-alumina + $MgAl_2O_4$(spinel) evolved from modification treatment after high temperature calcinations. By applying uniaxial compression tests and Weibull analysis it is clear that current reaction significantly improves the mechanical performance of the material. Ultrasonic impregnation proved more effective to obtained increased mechanical performance compared with incipient wetness impregnation. A trade-off between surface area and tensile strength is apparent for modified material. However one sample proved it possible to obtain strengths sufficient enough for proppant application in combination with open pore volume and surface area. Small $MgAl_2O_4$(spinel)- crystallite sizes is required to retain surface area and open porosity after high temperature calcinations. The mechanical performance is more dependent on homogeneous distribution of precursor during preparation, than impregnated nominal metal oxide- concentration and final crystallite sizes.

It is suggested that pore diameters and size distribution governs precursor distribution along with local metal oxide concentrations deposited during preparation and drying. Current work illustrates that it is possible to develop materials that fulfills requirements for multifunctional proppant applications. Results also imply that further improvement of the desired material properties is within reach.

Keywords: *Proppant, catalyst support, spinel, incipient wetness impregnation, ultrasonic impregnation, Weibull analysis, crush resistance uniaxial compression, tensile strength, stress distribution, nano- porous, alumina, spheres, mechanical performance, metal oxide distribution, pore diameters, pore size distribution, surface area, open porosity, proppant requirements*

Sammendrag

Over det siste tiåret har utnyttelsen av ukonvensjonelle reservoarer økt drastisk som følge av teknologiske fremskritt innenfor horisontal drilling og fler stegs- oppsprekking. Brønner som før ble ansett å være utenfor kommersiell rekkevidde, produserer i dag olje og gass konkurransedyktig. I årene som kommer er det spådd at andelen energi fra unkonvensjonelle kilder kommer til å fortsette å vokse forhold til konvensjonelle kilder.

"Proppanter" er sentrale komponent i hydraulisk oppstrekking ettersom de er plassert de hydraulisk induserte sprekkene og tilbyr økt permeabilitet i de ugjennomtrenglige stein-formasjonene tilstede i ukonvensjonelle reservoirer. Ved å endre proppant materialets mekaniske, fysiske, reaktive og geometriske egenskaper kan produksjon i oppsprekkede reservoar effektiviseres.

Utvikling av et strekt nano- porøst materialet åpner opp muligheten for "multi- funksjonelle" proppant- produkter. Proppant- materialer med høyt overflateareal plassert i oppsprekkede brønner med høy temperatur, kan muliggjøre katalytiske reaksjoner på proppant -overflater og demed "in- situ oppgradere hydrokarboner til mer verdifulle produkter. Et proppant produkt med høy grad av åpen porøsitet vil kunne impregneres med surfactanter som kan redusere friksjonen mellom olje og proppanter og føre til raskere olje- migrasjon i sprekker. Høy mekanisk styrke er et helt sentralt krav stilt til proppanter som skal kunne motstå "lukke- trykk" påført via flatene i sprekkene.

Eksperimentelle målsetninger var å oppnå best mulig kombinerte egenskaper av styrke, overflate areal og åpen porøsiet ved å justere synteseparametere og preparerings- metoder. Dette arbeidet undersøker modifisering av porøse γ-alumina kuler. Modifisering skjer ved impregnering av magnesium- oksid forløpere som ettererfølges av kalsineringsbehandlinger. To forskjellige metoder er benyttet for impregnering av de porøse alumina aggregatene. Primært er tradisjonell "incipient wetness impregnering" benyttet, men det er også eksperimentert med å bruke ultrasoniske bølger til å bistå impregnering.

Resultater viser at fase- sammensetningen: α-alumina $+ MgAl_2O_4$(spinel) fremtrer etter modifikajsonsbehandlig. Ved hjelp av enaxial kompressions testing og Weibull anlayser, blir det bevist at den aktuelle reaksjonen drastisk øker den mekaniske styrken til materialet. Ultrasoisk impregnering viste seg å være den mest effektive preparerings metoden for å oppnå høy mekanisk styrke. Et kompromiss mellom stryke og overflateareal er klart fremtredene for modifiserte materialer. En prøve beviser likevel at det er mulig for kandidatmaterialet å oppnå tilstrekkelig stryke påkrevd for proppant applikasjoner i kombinasjon med overflateareal og åpen porøsitet. For å beholde overflateareal og åpen porøsistet etter høy temperatur kalsinering er minst mulig $MgAl_2O_4$(spinel)- krystaller ønskelig. Høy mekanisk styrke vises å være mer avhenging av distribusjonen til forløpern under prepparering, enn krystallitt størrelser i produktet.

Det foreslåes at pore diameter og pore strørrelsesdistribusjon blant annet bestemmer forløper distribusjon og lokal metal- oxid fordeling under impregnering og tørking.

Dette arebeidet viser at materialer med egenskaper påkrevd for multi- funksjonelle proppant formål kan utvikles basert på kandidatmaterialet. Resultater indikerer også at videre forbedring av materialets egenskaper er innenfor rekkevidde.

Table of Content

1 Introduction

1.1 Background

According to British petroleum`s energy outlook [1], global energy demand are projected to grow 36% between 2011 and 2030. Key drivers for growing energy demand are expected population and income growth. World population is projected to reach 8,3 billion in 2030, which means an additional 1,3 billion people will need energy. Low and medium income economies are expected to account for over 90% total energy demand growth due to their population growth and rapid industrialization, urbanisation and motorisation. Today, coal offers the cheapest energy alternative in developing countries among others. Burning coal emits twice as much CO_2/kWh compared with natural gas [2]. Replacement of coal with natural gas could provide environmental benefits and carbon dioxide reduction the next coming decades while waiting for even better alternatives [2]. For a replacement of coal to occur, both natural gas prices and supply must be in a competitive position relative to coal.

High oil price- driven technological advances have recently led to the "shale revolution", first off for gas and then for oil. In 2000 shale gas provided 1% of U.S natural gas production, by 2010 it had increased to over 20%. The United States is now self sufficient in terms of natural gas supply, with significant export potential. Predictions say that shale gas and tight oil production will grow 3 fold, and over six fold respectively from 2011 to 2030. Together they are expected to account for a fifth of the increase in global energy supply to 2030 [1]. When the U.S shale gas production raped up in 2000, it began to displace coal in the power sector. This led to a big reduction in carbon dioxide emissions [2].

Main technological drivers for recovery in unconventional energy resources are directional drilling and hydraulic stimulation. Natural gas is contained in fine, isolated porosity and adsorbed onto other organic constituents contained in the shale. The relatively impermeable nature of the shale requires creation of additional surface area to retrieve trapped natural gas in commercially viable quantities[3]. Directional drilling increases recovery rates by accessing longer distances of the shale formations (up to 3 km) and intersecting fractures along the directional section.

Hydraulic stimulation or "hydro-fracturing" is a critical technology for creating and maintaining high permeability paths for resource recovery over the life of a well. This is commonly achieved by introducing a fracturing fluid consisting of surfactants, corrosives, and about 10% aggregates under high pressure to introduce and maintain fractures spreding from the well bore. The aggregates are locked in place by closure stress after stimulation pressure has been relived and "prop" the fractures open. Aggregates therby provide an open pathway for oil and gas to migrate towards the well bore for subsequent extraction. Hence, the aggregates are commonly referred to as "proppants" in the industry[3].

The shale revolution has resulted in a tenfold increase in proppant demand from 2000 to 2011. [4] Demand is projected to grow further to exceed 45 megatons per year by 2017.

During the last six decades many different materials has been used as proppants, including walnut hulls, Brady and Ottawa sands, glass, sintered bauxite and kaolin, and fused zircon. Current state-of- the- art proppants are manufactured from high-grade bauxite and kaolin. In deep wells, high-grade sintered bauxites and kaolin are preferred to satisfy the high strength required from the propping agent as closure stress easily surpass 10 000 psi, and and also over 20 000 psi (140 MPa) in extreme cases. To achieve optimal permeability in fractures, several material and geometrical

properties is required from proppants along with high mechanical integrity. Improvement of these properties could contribute to increased production effectiveness in unconventional oil and gas fields. This could make natural gas more available over time and increase the market share of natural gas on the expense of coal.

1.1.1 Multi functional proppant solutions

Traditionally proppants are only used to "prop" open fractures by resisting closure stress, and provide permeable pathways for oil and gas migration from the shale formation to the well bore. Future proppant solution could hold multi- functional purposes that further increase the effectiveness of unconventional resource- recovery.

1.1.1.1 Catalytic proppants

A catalyst support is a solid material with a high surface area to which a catalyst is affixed. Catalytic reactions occur on the surface atoms of a heterogeneous or nano material -based catalyst. Consequently, great effort is made to maximize the surface- area of a catalyst support to ensure large reactive area. In the petroleum's industry, a catalyst is used either for cracking or upgrading hydrocarbon chains.

High pressure and temperature that is present in some down hole environments, may enable catalytic reactions to take place in- situ if catalysts where to be placed directly into the reservoir fractures. This would add value to the unconventional reservoir either by increasing the total possible recovery and quality of the product, or by increasing well conductivity. In tight, oil rich reservoirs, catalytic proppants may be applied to crack down hydrocarbon molecule chains to shorter molecules in order to reduce viscosity of the fluid and thereby increase oil migration rate trough the proppant pack. In shale gas- rich reservoirs the catalytic proppants could be applied to upgrade hydrocarbons to longer more valuable molecule chains. High surface area is an essential requirement for catalyst supports, hence also equally important for a catalytic proppant to function properly.

1.1.1.2 Surfactant carrying proppants

Today, various chemicals and surfactants are used to enhance oil recovery. Usually as dilute solution, they are used to aid mobility of hydrocarbons. Surfactants are compounds that lower the surface tension between to liquids or between a liquid and a solid. Injection of alkaline or caustic solutions into reservoirs with oil that has organic acids naturally occurring in the oil will result in production of soap that may lower the interfacial tension enough to increase production rate and potential. Dilute solutions of surfactants such as petroleum sulfonates or bio- surfactants such as rhamnolipids may be injected to lower the capillary pressure or the interfacial tension that impedes oil droplets from migrating through a reservoir [5].

Traditionally, production enhancement surfactants are injected with a secondary "pushing well" to sweep oil out of the reservoir and up the production well. With a nano- porous proppant, production-enhancing surfactants can also be carried within the porous structure of the material

and placed into fractures. Surface tension drop between hydrocarbons and proppants might then reduce the friction between the two compounds, increasing the production rate.

For this to be possible, a high degree of open porosity is required of the proppant material to allow surfactants to be infiltrated and stored within the porous structure.

2 Aim of the work

Previous investigations of γ- alumina, modified with a metal oxide precursor and subsequent heat treatment, have proven to increase the attrition resisitance of the current alumina based material [6]. The intended use of the material was then as a catalyst support. The increase in attrition resistance occurs as a result of the reaction between the γ- alumina and the impregnated metal oxide that transformes into spinel phase and α- alumina (ss) after calcination.

Internal work from recent semester focused on finding required properties proppants must inhibit, and investigates different tests methods to evaluate these properties. The uniaxial compression test and Weibull analysis of recorded data was among others found effective in evaluating material tensile strength and reliability.

Central objective of this work was to optimize synthesis parameters such as MgO- content impregnated, impregnation- method and calcination temperature. The target was to achieve highest possible combination of material strength, suface area and open porosity for the candidate material. Also other parameters that would affect the well performance in operation for the candidate material is evaluated and compared to a commercial resin coated proppant product.

Also an objective was to evaluate the possibility of using the material for multi- functional proppant applications. For this evaluation surface area and open pore volume was investigated as a function of different synthesis parameters. The overall goal of the investigation was to find correlations between synthesis parameters, methods and material properties required for multi-functional proppant application.

3 Literature review

3.1 Proppants & reservoir conditions

The operating environment is constantly acting on the proppants down hole and driving degradation of proppant properties resulting in decreased permeability. The down hole- conditions are thereby important to address and quantify, to properly evaluate if proppants inhibit adequate properties to resist this harsh environment over time [4].

The most important requirement for propping agents is their ability to resist closure stress that occurs when fracture stimulation pressure is pulled back. Proppants will then keep the fractures open and provide a permeable pathway for oil and gas migration. Operators usually start with evaluating the closure stress the proppants will be subjected to along with the desired conductivity at these stresses. If proppants are not capable of withstanding the closure stress the material will crush and generate fines that will block the permeability of a proppant pack over time. Fines are small particles originating either from crushed proppant material or formation. According to SPE by Colter et. al a 5% generation of fines could reduce flow trough fractures by 60%. If large amount of proppants crush, the fractures will close completely [7].

Figure 3.1: *Illustration of proppants deployed in a fractured reservoir, and fines generation introduced by crushing of proppant under high closures stress (F).*

In- situ closure stress acting on proppants may be calculated from values measured of true vertical depths and fracture gradient. According to SPE 136338, the correct way of determining closure stress is by equation 3.1 below.

$$\boldsymbol{\sigma_{prop} = \left(g_f * D\right) + \Delta p_{drawdown}} \quad \textbf{\textit{(Eq. 3.1)}}$$

In- situ closure stress acting on proppants,
σ_{prop}*: Closure stress*
g_f*: Fracture gradient*
D*:Vertical depth*
$\Delta p_{drawdown}$*: Reservoir drawdown pressure*
$\Delta p_{drawdown} = p_r - p_{wf}$
p_r*: Reservoir pressure*
p_{wf}*: Flowing bottomhole pressure (FBHP)*

In- situ closure stress acting on proppants normally ranges between 2000- 15000 psi (*14- 105 MPa*) and temperature is commonly in the regime 38 to 138℃. In some extreme high-pressure, high temperature reservoirs (HPHT), closure stress can reach 20000- 30000 PSI (*140 MPa*) and

temperature up to 260℃ [8]. Increased partial pressure of CO_2 and H_2S, lower the pH value. This may also contribute to degradation of proppants over time.

Theres several different proppant products on the market today, designed to withstand degradation in different environments. These proppants can be categorized as following [7]:

- Brandy (brown) sand
- Ottawa (white) sand
- Lightweight, intermediate and high density (bauxite) ceramics
- Pre-cured resin coated sand and ceramics
- Curable resin coated stand and ceramics
- Newer proppants that combine light weight and high strength through the use of nano-structuring

Brandy and Ottawa sand offers the cheapest alternative for lower range closure stress application in gas reservoirs. Ottawa sand is more spherical and more crush resistant than brandy sand, and its less expensive than ceramics and resin-coated product. For slick water fractures Cheakespare energy reports that Ottawa sand is the most cost-effective proppant. Man- made ceramic products are typically applied in intermediate to high closure stress environment, where sand either offers insufficient crush resistance and/or low base- permeability. Pre- cured resin coated products offers a hydrophobic outer layer that reduces friction between fluid and proppants. This trait is desirable in oil rich reservoirs. The resin- coated products also offer less fines production in operation, due to the encapsulating properties of the resin. Curable resin coated products add an additional function to the proppant solution. These products cure in- situ after placement in the fracture due to the high temperature environment, thus they create a consolidated pack. A consolidated pack offers resistance against costly proppant flow back and back production under cyclic loadings that are induced by fracturing stimulations treatments. Newer nano structured proppant- materials are meant to provide a high conductivity for extreme high closure stress and high temperature environment. Cheakespare energy has for now evaluated these products to be cost prohibitive [4, 7].

Proppants are deployed in different sizes depending on closure stress, type of reservoir and the required permeability. Typical sizes are between 8-140 mesh corresponding to sphere diameters of about 106 μm – 2.36 mm [4]. Table below show commonly used proppant sizes and their base permeability without applied closure stress [9]. Permeability will decline faster for larger diameters proppants when increasing load are applied due to weakest link- mechanisms (Described in section 3.4).

Mesh size	Diameter (μm)	Proppant permeability (Darcy's)
12/20	840 - 1573	450 (+)
20/40	420 - 840	120
40/60	314 - 420	60
70/140	106 - 212	0.6

Table 3.1: *Commonly used mesh sizes, corresponding particle diameter and permeability without applied load.*

3.2 Required properties

Properties required to achieve highest possible fracture conductivity can be reasoned from basic physical laws that describe various permeability- dependent relationships. Most central is Darcy`s law, which provide a simple proportional relationship between instantaneous discharge rate of a fluid through a porous medium, the fluid viscosity and the pressure drop over a distance. Darcy's law may be applied to provide a basic approach to proppant pack conductivity calculations.

$$Q = \frac{-kA}{\mu} \frac{(P_b - P_a)}{L} \quad \textbf{(3.2)}$$

*(**Eq. 3.2**: Darcy`s law)*

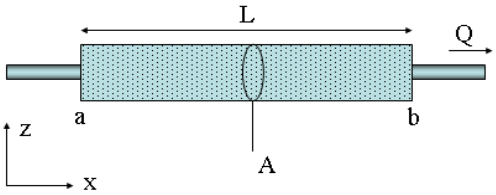

***Figure 3.2:** Schematically illustration of Darcy`s experimental set up for measuring discharge rate.*

The total discharge rate Q (unit of volume per time, m^3/s) is equal to product of the permeability of the medium, k (m^2), the cross section area, A (m^2), and the pressure drop $(p_b - p_a)$, all divided by the product of the viscosity $(Pa * s)$ and the length where the pressure drop is occurring. Fluid migrates from high to low pressure regions. Proppants can contribute to increase the total discharge rate in fractures by achieve higher values for medium- permeability, k and cross section area, A. The cross section area is dependent on the fracture width w_f, which is increased by using proppants with good transport abilities. Transport abilities are dependent on the particle settling velocity in fracturing fluids, and low-density particles are desirable to lower settling velocities which increase proppant transport and fracture widths.

Settling velocity of particles in fluids can be derived from Stoke`s law [10],[11].

$$V = 1.15 * 10^3 * \left(\frac{d_{prop}^2}{\mu_{fluid}}\right) * (\rho_{particle} - \rho_{fluid}) \quad \textbf{(3.3)}$$

*(**Eq. 3.3**: Settling velocity of particles in a fluid)*

$$\boldsymbol{V}: Settling\ velocity$$
$$\boldsymbol{d_{prop}}: Proppant\ diameter$$
$$\boldsymbol{\mu_{fluid}}: Viscosity\ of\ the\ fracturing\ fluid$$
$$\boldsymbol{\rho_{fluid}}: Density\ of\ the\ fracturing\ fluid$$
$$\boldsymbol{\rho_{particle}}: Density\ of\ proppant\ particles$$

As seen from eq. 3.3, lower settling velocities are obtained for smaller diameter particles with low particle densities and by using higher viscosity fracturing fluid.

Permeability of the fracture (proppants / medium), k_f, may be approximated theoretically with equation 3.4 given below[12].

$$k_f = \frac{\phi^3 (d_p \Phi_s)^2}{72\lambda_m (1-\phi)^2} * \left(1 + \frac{d_p \Phi_s}{3(1-\phi) w_f}\right)^{-2} * (1 - DF) \quad \textbf{(3.4)}$$

Eq. 3.4*: Fracture permeability approximation*

$\boldsymbol{k_f}$*: Fracture permeability* (L^2)
$\boldsymbol{\phi_m}$*: Matrix porosity (void space between proppants)*
$\boldsymbol{d_p}$*: Proppant diameter (L)*
$\boldsymbol{\Phi_s}$*: Sphereicy*
$\boldsymbol{w_f}$ *: Fracture width (L)*
$\boldsymbol{DF}$: *Proppant degradation factor*

Fracture width in terms of concentration per unit area is: $w_f = \left(\frac{C_a}{[\gamma \rho_0 (1-\phi_m)]}\right)$, where C_a, is the proppant consentration per unit area, γ is the particle density, and ρ_0 is the reference density of water (4℃). For $\phi_m < 0.5$, $\lambda_m \approx \frac{25}{12}$ (typical value). The proppant degradation factor is a quantification of degrading effect that occurs over operational time. It is defined:
$DF = 1 - \left(\frac{k_f}{k_{teo}}\right)$, where k_{teo}, is the undamaged permeability.

When designing a fracture, proppant selection is often based on the dimensionless fracture conductivity constant, F_{CD}. Values of $F_{CD} > 10$ are desired for sufficient fracture conductivity. To achieve this value, high k_f-values is preferred. This constant is based on the contrast between the flow capacities (permeability) of the fracture, and the surrounding reservoir permeability (formation permeability) [13].

$$F_{CD} = \frac{k_f w_f}{k_m L_f} \quad \textbf{(3.5)}$$

Equation 3.5*: Dimensionless fracture conductivity constant*
$\boldsymbol{k_m}$*: Formation permeability,* $[L^2, md]$
$\boldsymbol{L_f}$*: Fracture half- length (distance from wellbore to tip), [L, m]*

Deduced from the equations in this subsection, preferred proppants/ material properties can be summarized as:

- **High mechanical integrity (Crush resistance):** High strength is a key trait to obtain the structural integrity of fractures, and reduce production of permeability- blocking fines from crushed material. High crush resistance will also make sure fracture widths are kept intact. This will ensure a low proppant degradation factor (DF) and higher fracture permeability over time. Resin coated products offer encapsulation of fines and lower degradation factor as mentioned. However, if material strength is insufficient, proppants will flattens and pack together under high closure stresses. This reduces both fracture widths and matrix- porosity and will thereby increase the degradation factor even for circumstances where a minimum of fines has been produced.

- **Chemically inert:** HCl and HF are occasionally pumped down hole to remove near-wellbore damage in many types of wells. This imposes requirements in acid solubility resistance for the specific proppant product applied. Proppant dissolvent due to acidic exposure will greatly increase the degradation factor (DF). High acid solubility may cause wider size distribution of proppant spheres leading to reduction in matrix porosity. Also mechanical strength could be reduced causing smaller fracture widths and more permeability- blocking fines. S.K Cheung et al. (1988) concluded that HCl does not significantly dissolve bauxite materials, but HF/HCl acidic mixtures do. Rate of dissolvent increases with higher HF concentrations. ISO-13503-2 standard test contain an acid solubility test along with other proppant quality test methods.

- **Low particle density:** Seen from equation 3.3, low particle density decreases settling velocity and improves transport abilities for proppants. Lighter particles can be placed into fractures in larger concentration yielding bigger fracture widths, as seen from the equation: $w_f = \left(\frac{C_a}{[\gamma \rho_0 (1-\phi_m)]}\right)$

- **Round and spherical:** As seen from equation 3.4, roundness, spherical shapes and matrix porosity influence the fracture permeability. Round and spherical particles will give less dens proppant packing and increase interstitial void space in between each sphere, providing an open path for oil and gas migration.

- **Narrow size distribution of proppant particles:** Size distribution of particles also affects the matrix porosity and fracture permeability. A narrow distribution of particles is desired to obtain high matrix porosity.

3.3 ISO standard tests

ISO-13503 is a compilation of earlier API RP 56, API RP 58, and API RP 60- tests for conductivity evaluation and quality assurance of proppants. Evaluations performed in this work that are in accordance to ISO-13503-2 [14] for quality assurance, are rather qualitative. More extensive testing with methods described in ISO- 13503-5 [15] are required to fully confirm and evaluate conductivity properties.

- **ISO-13503-2** has been developed to improve quality control of proppants at well sites.

- **ISO-13503-5** deals with procedures for measuring the long- term permeability of proppants in laboratory scale. The reason for the test is to obtain better information about actual permeability performance and check proppants ability to resist various degradation mechanisms over time. The including “wet hot crush test” is a modified version of Darcy`s experiment but with additional high temperature and crushing load applied.

3.4 Mechanical mechanisms

3.4.1 Weakest link theory (Weibull theory)

Weakest link theory describes structures where failure of one element within a volume leads to failure of the whole structure. W. Weibull first described this size effect mathematically. He proved that only a power law with a threshold could describe the tail of a statistical distribution in the region of extremely low failure probabilities. Once a statistical distribution of local strength is established, the probability that the whole structure fails under a given load can be evaluated. For chainlike structures such as wires and ropes, the probability of failure is simply the probability that there exist at least one link whose strength is lower than applied stress. Extension of this concept to structures under non- uniform stress reveals that for geometrically similar structures with different sizes D, the nominal strength is a power function of D with a negative exponent:

$$\sigma_N = \sigma_{N0} * \left(\frac{D}{D_0}\right)^{-\frac{n}{m}} \quad (3.6)$$

***Eq. 3.6**: Weibull power function*

In eq. 3.6 D_0 is a fixed refrence size, σ_{N0} is the corresponding nominal strength, n =3 for three dimentional similarities and m is the Weibull modulus that characterizes the strength distribution for the particular material [16].

Weibull theory explains size effect phenomena on strength by the random distribution of local material properties. The probability of finding a weak spot in a large volume structure is higher than for smaller structures. Of that reason, bigger structures fail at lower stress levels than smaller ones.

Weibull approach is well adapted to evaluate mechanical properties of ceramic material such as the alumina spheres investigated in this work, as pre-existing flaws in the particle microstructure affect the failure- level (Weibull, 1939,1951). The crack propagation mechanisms is of less importance since the elastic strain energy required for initiating a crack far outweighs the energy required for it to propagate. Weibull distribution is based upon that when a fracture first is initiated within a specimen, it leads to a global failure immediately. Ceramic material tend to have wide strength distributions due to the high correlations between structural strength and random flaws/defects [17],[18].

3.4.2 Elastic modulus & porosity

Porosity and the presence of inclusions affect the mechanical properties of ceramic materials. Porosity increase always results in decrease in elastic modulus. MacKenzie has derived a relationship between elastic modulus and volume fraction of pores in ceramic materials [19].

$$E = E_0 * (1 - 1.9P - 0.9P^2) \quad \textbf{(3.7)}$$

Equation 3.7: Effect of porosity on elastic modulus

E_0, is the elastic modulus of non-porous material and P is the volume fraction of pores. This approximation is generally valid for materials containing up to 50% porosity and having poissons

ratio of 0.3. The severity of the strength reduction in ceramic materials is dependent on several additional factors such as: pore geometry, distance between pores, pore- overlapping, distance between pores and surfaces, the presence of cracks of grain boundary cusps adjacent to a pore and size and shape of inclusions[19].

Because of all factors affecting the elastic modulus of porous materials, a fairly accurate relationship between porosity and elastic modulus over an entire porosity range (>50%) has proven difficult to obtain[20],[21].

3.4.3 Stress distribution and fracture behaviour in brittle spheres under uniaxial compression

Hiramatsu and Oka [22], developed an efficient method for testing the mechanical properties of rocks by investigating the strength of irregular shaped pieces. They assumed that the stress distribution in a solid, irregular shaped specimen under diametric compression was the same as in a spherical specimen. The maximum stress was reported to occur on the central axis between the two loading points. Li et al. [23], successfully applied the approach of Hiramatsu and Oka to calculate the tensile strength of solid catalyst supports of spherical shape. By using Weibull statistics, Li showed that all test specimens revealed the same fracture mode and that failure was due to tensile stresses. Kshinka et al.[24] Investigated glass spheres under compression and observed explosive like fractures. The samples were completely pulverized at failure and no conclusion about fracture mode or crack origin is deduced from the debris. However, by using Weibull statistics the authors managed to show that fracture origin most likely came from the bulk phase of the material, and not the surface. Shipway and Hutchings[25] presented a numerical method to determine the stress distribution within brittle spheres under uniaxial compression and investigated fracture of lead glass spheres under same conditions[26]. This work was based on investigation and calculations of stress distribution in spheres carried out by Dean et. al. [27]. The work showed that maximum tensile stress occurs in the interior of the specimen, as suggested by previous investigations. Furthermore, the stress distribution also depends on the ratio between the radius of the contact area between the platen and the sample a_c, and the sample radius R. Figure 3.3 show the relative development of tensile stress along the axis and the surface of spherical test specimens with increasing contact area between the specimen and the platen which is denoted, $\frac{a_c}{R}$ after Shipway and Hutchings[25].

It this figure it is evident that for values $\frac{a_c}{R} < 0.6$, the axial tensile stress exceeds the surface tensile stress. Given a homogenous distribution of flaws, the particle will fail due to tensile stresses occurring in the centre of the specimen, rather than the specimen surface. M. Bernhardt [28] used the same arguments in his work on lightweight aggregates.

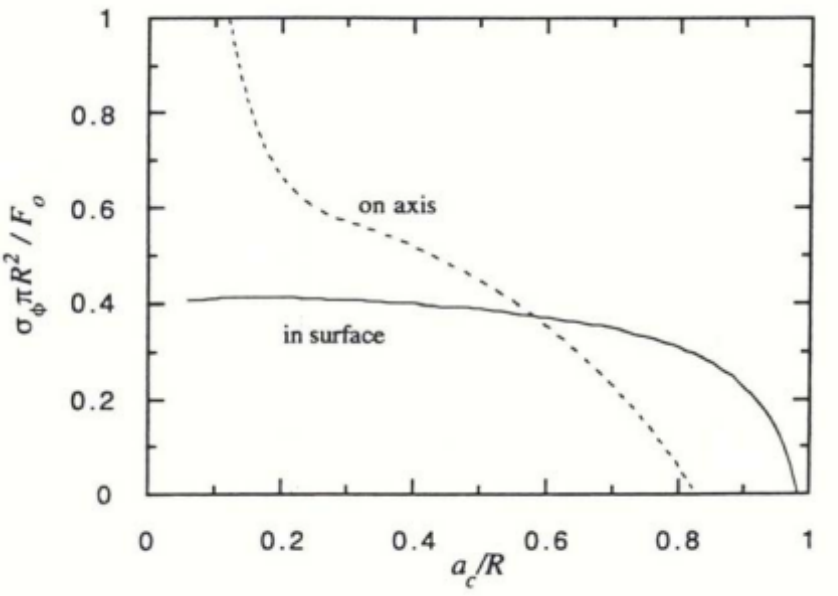

Figure 3.3: *Relative tensile stress on axis between loading points and specimen surface of a brittle sphere under compression. Fraction of stress distributed on axis and surface, is dependent on the ratio of the radius of the contact area between platens and specimen radius. At*

3.5 Microstructure and mechanical properties of porous alumina

Rotan [6] investigated different modifications of alumina based catalyst supports and phase compositions and microstructure associated with mechanical properties. The purpose of his work was to find the fundamental mechanisms that led to enhanced attrition resistance, in order to further improve the durability of alumina based catalyst- support materials. In his work he showed that by impregnating porous γ - alumina supports with different metal oxide salt precursors, the alumina would react with the metal oxide and form a spinel phase that could form a metastable solid solution with the γ - alumina. The initiation and the extent of the reaction proved strongly dependent upon the chemical nature of the metal oxide and the calcination temperature. Highest reaction rates were found for modifications with NiO and MgO, where the $\gamma -$ alumina started to react with the metal oxide around 500- 600℃ in air.

Furthermore, Rotan`s experiments showed that the reaction between the alumina and metal oxide had strong impact on the final microstructure of the modified catalyst support. In samples where the metal oxide had reacted with the alumina at low temperature (such as with NiO and MgO) the final microstructure consisted out of significant amount of relatively small spinel crystallites and $\alpha -$ alumina. The amount of metal oxide impregnated also affected the final microstructure. Vickers hardness indention performed reveald that those samples with increased hardness relative to pure γ- and α - alumina where those with microstructure containing significant amounts of small spinel crystallites.

Rotan concluded that the increase in mechanical properties was related to strong intergranular bonds that formed between the small spinel crystallites and the α-alumina phase. He also proposed that in high temperature, coarsening of spinel crystallites enlarges the contact area between the adjacent crystallites that forms a rigid network that increase the hardness and attrition resistance.

A hypothesis for the mechanisms that governs the precipitation of α- alumina from the metastable solid solution was also presented in Rotan`s work. The suggestion is that because both the spinel and α- alumina crystal structures are based on close packed anions, a rearrangement of oxygen anions from an ABCABC… stacking to ABAB… stacking in the transition between the spinel and α- alumina phases is plausible. This mechanisem was the proposed to further enhance the intergranular bonding of α- alumina and spinel phases. In addition, the different in thermal expansion between the two phases could result in a harning effect where the spinel crystallites are under tension and α- alumina is under compression.

4 Experimental

4.1 Sample preparation

Two different impregnation methods were applied in this work. Incipient wetness is a well-known standard method for modifying catalyst support materials by impregnation of metal oxides. The ultrasonic impregnation method was an idea that appeared after some attempts to measure open pore volume for samples. Standard Archimedes measurement was challenging to perform, because of the very small spherical specimens at scope. Therefore, a way around the standard measurement method was needed to obtain reasonable values for the volume fraction of open porosity (which is an important measure in this work). In atmospheric pressure, water did not completely enter the porous alumina structure. Air bubbles cringed out the alumina spheres for days when soaked in a container with distilled water, meaning that pores did not fully fill up. However, by placing the container with the alumina spheres soaked in distilled water in an ultrasonic bath, bubbles ceased to tickle out of samples in about 30 minutes. Due to this observation, an experiment with using ultrasonic aided impregnation was carried out in order to achieve a more homogeneous distribution of metal oxide within the porous alumina skeleton. Subsequently, similar experiments were found in literature, where the ultrasonic treatment has proved to improve metal oxide dispersion [29, 30].

4.1.1 Components

- **Support material (γ- alumina spheres)**

Nano porous γ- alumina spheres provided by Sasol are used as base material in this work. The material is made from high purity nano- sized boehmite powder. By using the surface tension of oil, the nano- porous spheres are formed in an industrial process. Table 4.1 show the physical and geometrical properties of the base material at scope.

Properties:	Unit	γ- Alumina spheres (Type 1.0/160)	γ- Alumina spheres (Type 1.8/210)
Diameter (d_{30})	[mm]	1,108	1,735
Crush strength	[N]	Min. 45	Min. 50
Apparent Bulk Density	[g/l]	740-820	540-580
Surface Area	[m^2/g]	150-170	211
Pore Volume	[ml/g]	Min. 0.45	Min. 0.75
Particle Density	[g/cc]	1.34	0.97
Particle Porosity	[-]	0.665	0.76

***Table 4.1**: Physical and geometrical properties of Sasol alumina spheres, size 1.0 & 1.8 mm [31].*

- **Metal oxide precursor**

Magnesium nitrate hexahydrate from Sigma Aldrich is the metal oxide used in modification of alumina spheres in this work. Content in wt.% is given in table 4.2.

Magnesium – nitrate hexahydrate	Molecular weight:	Substances	Wt. %	In oxides:	Wt. %
$MgN_2O_6 * 6H_2O$	256,4 g/mol	Mg	9.48	MgO	15.72
		H	4.72	H_2O	42.16
		N	10.93	H_2O_5	42.12
		O	74.88		

Table 4.2: *Specifications for Sigma Aldrich magnesium nitrate hexahydrate*

4.1.2 Incipient wetness impregnation

Preparation steps are presented in figure 4.1 and may be summarized as following: Support material is first dried prior to impregnation. A salt precursor solution is then mixed in right concentrations to obtain desired nominal wt.% ratio of support material and metal oxide. The dehydrated pellets (support) are placed in a container and the solution is slowly added to the support material and capillary forces pull the liquid solution into the pores. All of the solution should have been added at the point of which the pores are statured as evident by the beading of excess solvent. In such event the precise amount of solution is assured to be present in the support. Drying either in air, inert gas or vacuum follows the impregnation and the precursor crystallites are deposited inside the pores.

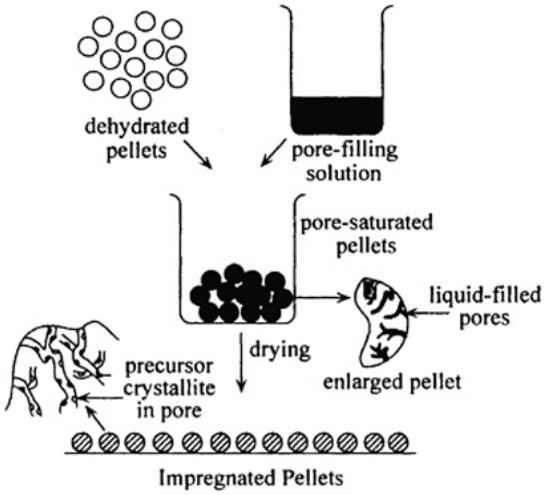

Figure 4.1: *Illustration of the incipient wetness preparation procedure applied in this work. Adapted from ref.[32]*

γ- Alumina support were prepeard using a one- step incipient wetness method to disperse metal oxide into the porous structure. Four batches were made with this technique, and was carried out with following steps:

1. **Determination of water absorptivity**

Water absorptivity (amount of water to fill pores) was initially determined for the 1.8/210 and 1.0/160 type spheres. An evaporating dish and a spatula were first weighted with a technical balance (accuracy 0.01g). Samples were then accurately weighted out using the same balance. Sample support (alumina spheres) was poured into the evaporating dish and the total weight was recorded (weight of support+ evaporating dish+ spatula).

Small amounts of distilled water was then added drop wise with a pipette and mixed with the support material using the spatula. The evaporating dish was then knocked into the table approximately 20 times. These two steps were then repeated until a thin layer of water was visible upon knocking. This represents the point of incipient wetness, where pores are saturated with water. The evaporating dish including sample support, impregnated water and the spartula, were weighted again. The amount of water impregnated was then determined using the difference of weight before and after impregnation.

The amount of water adsorbed per gram of support was calculated according to equation 4.1.

$$Abs = \frac{m_{H_2O}}{m_{support}} \quad \textbf{(4.1)}$$

Equation 4.1: *Water- Abs calculation with incipient wetness.*

2. **Determination of the amount of solution (AS) to be used for incipient wetness impregnation**

An evaporating dish was weighted before support was added to the dish. Each batch consisted out of approximately 20 grams of alumina spheres before precursor solution was added. The amount of solution (AS) was calculated in accordance to equation 4.2.

$$AS = m_{support} * Abs \quad \textbf{(4.2)}$$

Equation 4.2: *Amount of precursor solution needed for incipent wetness impregnation.*

3. **Calculation and mixing of precursor**

The open pore volume of the alumina spheres predetermines the amount of liquid solution (AS) that can be impregnated. The consentration of magnesium nitrate in water was adjusted to obtain the desired nominal wt% compostition of alumina support and MgO. The total amount of metal oxide that can be placed into the support material in a one-step incipient wetness procedure is limited by the solubility of the nitrate in water, and the open pore volume. The amont of dry salt precursor to be mixed into the water solution was dertermined with respect to wt % metal oxide

the dry precursor holds, relative to the weight of the support. In example: The dry precursor contains 15.72wt% MgO. Thus, ten grams of support needs to be impregnated with ten grams of metal oxide precursor mixed with distilled water to achive approx. 14wt % MgO content relative to the support. The solubility of magnesium nitrate hexahydrate in water is 125g/100mL.

4. **Impregnation**

The calculated amount of dry precursor needed for a batch was the placed into an evaporating dish and mixed with destilled water to obtain the predetermined AS (ml) required to fill up the pore volume to the point of incipient wetness.

Following batches were prepared with incipient wetness: Sphere- type 1.0/160 was impregnated with 5 and 12 wt.% MgO, and sphere-type 1.8/210 was prepared with 5 and 13 wt.% MgO.

4.1.3 Ultrasonic impregnation

The ultrasonic aided impregnation technique provides an alternative to the incipent wetness impregnation. The idea behind this experiment was that ultrasonic waves mechanically would aid the capillary forces that would result in a more homogeneous distribution of precursor solution within the porous structure of the support material. One batch of type 1.0/160 sphers was impregnated with 15wt% MgO using this technique. The procedure is based on the same principles as incipient wetness impregnation, but with a few modifications. Preparation of samples was carried out as described below:

1. **Determination of ultrasonic water absorptivity / open pore volume**

This step is basically to measure how much water support- material may absorb with ultrasonic aid (This amount is higher than without ultrasonic aid). To establish ultrasonic water absorbtivity, particle density must be measured in advance. Particle density is the density of each sphere including the internal porosity (measurements described in 4.3).

First a granulated cylinder and a glass spartula was weighted out using a technical balance. Alumina support was then added to the granulated cylinder and weighted out. Next, the sample (alumina support) is added to the granulated cylinder and weighted out again. The sample volume is calculated according to equation 4.4.

$$V_{sample} = \frac{1}{\rho_{particle}} * m_{support}\ [cm^3] \quad \textbf{(4.4)}$$

Equation 4.4: *Sample volume*

Destilled water with volume V_{water} was then added to the alumina support with the volume V_{sample}. If pellets (support) did not inhibit any open porosity when water was poured into the cylinder, the total containing water level would be the volume of the sample pluss the volume of water added to the granulated cylinder. This volume is denoted as the theoretical volume ($V_{teo}\ [cm^3]$).

$$V_{teo} = V_{sample} + V_{water}\ [cm^3] \quad \textbf{(4.5)}$$

Equation 4.5: *Teoretical volume, if the support material completely lacked open pore volume.*

The granulated cylinder containing destilled water, sample support and spatula was the placed in an ultrasonic bath for 35 minutes with occasional sirrings.

After the ultrasonic treatetment the cylinder was placed on a table and total waterlevel was read off and recorded. The cylinder was also weighted out again to correct for possible water loss. The difference between the theoretical volume V_{teo} and the new-recorded volume $V_{recorded}\ [cm^3]$ denotes the open pore volume of the sample, or the water contained inside the porous support material achieved with ultrasonic aid.

$$P_{sample.open} = V_{teo} - V_{recorded}\ [cm^3] \quad \textbf{(4.6)}$$

Equation 4.6: *Open pore volume of samples*

To obtain the water absorption (Abs), the sample open pore volume $P_{sample.open}$ must be dividen on the sample weight m_{sample}:

$$Abs = \frac{P_{sample.open}}{m_{sample}} \quad [\frac{cm^3}{g}] \quad \textbf{(4.7)}$$

Equation 4.7: *Ultrasonic- water Abs (open pore volume)*

2. Amount of impregnated solution

The calculated amount of solution (AS) is the same as for in incipient wetness impregnation (Eq.4.2). In ultrasonic impregnation the support material are placed into a pool of mixed precursor solution, instead of using the exact (AS) as in incipient wetness.

3. Mixing of precursor

Since the alumina support eventually ends up in a bath of precursor solution, only the desired precursor solution concentration needs to be determined regarding the final nominal composition of Mg- metal oxide and alumina.

4. Ultrasonic impregnation

After desired precursor concentrations was calculated and mixed in a container, the alumina support was poured into the precursor solution. The container was then placed in an ultrasonic bath for 30-35 minutes with occasional stirrings. After the treatment the excess precursor solution was poured out.

4.2 Heat treatment

Drying

Drying was performed on all batches prior and after impregnation in 90 ℃ for approximately 20 hours. A Termaks drying cabinet was applied.

Calcination

Six calcination programs were carried out in a Nabertherm furnace in air. All programs followed the same heating profile and holding times at final calcination temperature. The six different final calcination temperatures were: 1000, 1060, 1100, 1125 1140 and 1150℃. Samples were first heated up to 500℃ and held for four hours. From there, the temperature inclined to the final calsination temperature where samples were held for 8 hours. The samples were subjected to cooling rates of approx. -150℃/ hour. Profile for calcination programs are showed in figure 4.2.

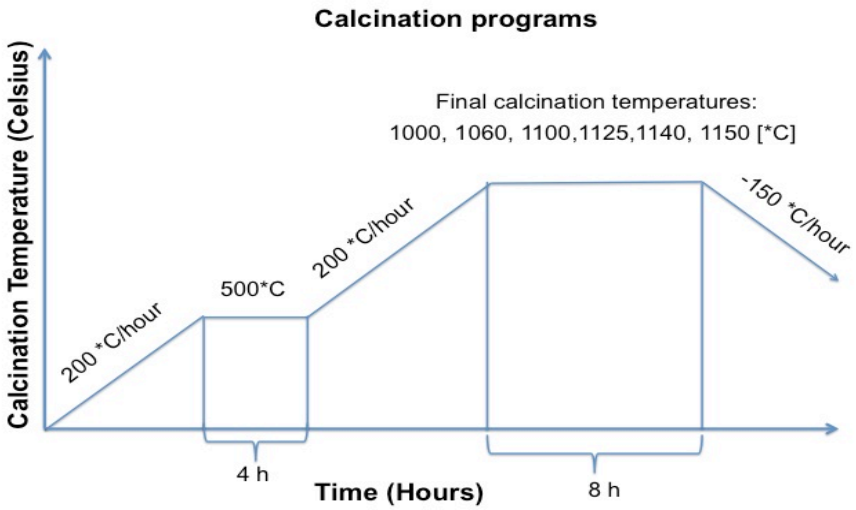

Figure 4.2: *Temperature profile for calcination programs*

4.3 Geometrical & physical properties

Average diameter was determined with a caliper for 35+ spheres in each sample. Approximately 100 spheres from each sample were then counted and weighted out, obtaining average weight per sphere. Average volume of spheres was calculated from the average diameter. Particle density was den obtained by using equation below. Particle density includes spheres with internal porosity.

$$\rho_{particle} = \frac{m_{average}(weight\ of\ one\ sphere)}{V_{average}(volume\ of\ one\ sphere)} \qquad \textbf{(4.8)}$$

Equation 4.8: *Particle density*

Theoretical density or crystallographic density was calculated using the nominal composition of samples $((1 - wt\%MgO) * wt\%Al_2O_3 + wt\%MgO)$ and corresponding crystal composition after calcination treatment read off the $Al_2O_3 - MgO$ phase diagram. The level rule was used to approximate amount of phases. Crystallographic phase- densities were obtained from XRD and given in the results.

$$\rho_{teoretical} = \rho_{phase\ 1} * X_{phase\ 1} + \rho_{phase\ 2} * X_{phase\ 2} + \rho_{phase\ n} * X_{phase\ n} \quad \textbf{(4.9)}$$

$$\text{Where; } \sum_{i=1}^{n} X_i = 1$$

Equation 4.9: *Theoretical density derived from amount of phases and corresponding crystallographic densities.*

Particle porosity was then calculated for each sample using equation 4.10.

$$\phi_{particle} = 1 - \frac{\rho_{particle}}{\rho_{theoretical}} \qquad \textbf{(4.10)}$$

Equation 4.10*: Particle porosity*

Bulk density ρ_{bulk} is defined in this work as the density including spheres, particle porosity and the porosity in-between spheres. Bulk density was determined by recording the weight and volume of samples that had been poured into a granulated cylinder. Results are listed in table 5.1 & 5.2 in results. $\phi_{particle}$ Represents the total porosity within a sphere. The amount of this porosity that occurred as open porosity was determined by measuring ultrasonic water absorptivity described in section 4.3.1. For each sample open pore volume was determined and compared with total pore volume.

By dividing bulk density on particle density, random close packing (η_{RCP}) was determined. This measure was later used in crush resistance calculations. Random close packing denotes how closely spheres are packed together. Matrix porosity ϕ_{matrix} was also determined from this measure.

$$\rho_{bulk} = \frac{m_{packed\ spheres\ in\ cylinder}}{V_{packed\ spheres\ in\ cylinder}} \ [g/cm^3] \qquad \textbf{(4.11)}$$

Equation 4.11: *Bulk density*

$$\eta_{RCP} = \frac{\rho_{bulk}}{\rho_{particle}} \qquad (4.12)$$

Equation 4.12: *Random close packing*

$$\phi_{matrix} = 1 - \eta_{RCP} \qquad (4.13)$$

Equation 4.13: *Matrix porosity*

Matrix porosity represents the void space in-between particles where oil and gas can migrate.

The degree of sphereicity and roundness was determined by visual inspection according to ISO-13502 [14]. Template for visual inspection is given in below.

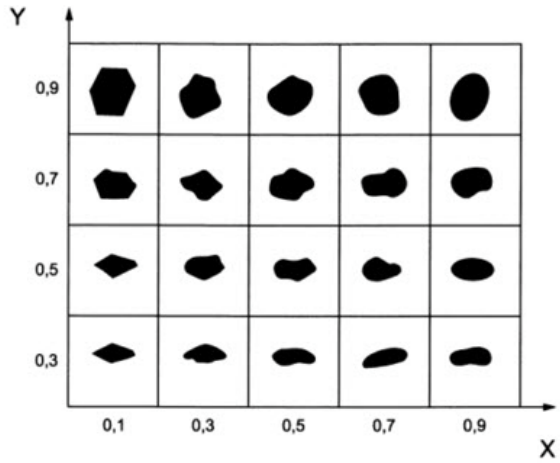

Figure 4.3: *Template for visual inspection of sphereicity and roundness, where Y-axis represents sphereicity and X-axis is roundness (smoothness).*

Results for physical and geometrical properties are given in table 5.1 and 5.2.

4.4 Mechanical evaluation

Methods and techniques applied for quantifying mechanical properties are described in this section. Weibull analysis and crush resistance calculations are the most central part in evaluation of mechanical properties.

4.4.1 Uniaxial compression & tensile strength approximation

Strength measure for samples were obtained by applying uniaxial compressive load on single spheres, and record the load at failure. Tests were performed with an Instron 5543 device mounted with a load cell capable of 10 kN. Software settings were entered first. All tests were performed in load control mode, where load was applied with a rate of 10 -130 Newton per minute. Loading rates were determined by the strength of the material at scope, where higher strength materials were tested with higher loading rates. End of testing/ compression were set with an "end of compression load sensitivity" of 40%. To enable accurate measure of compressive extension of the piston for each test, auto balance settings were set. Test setup is illustrated in figure 4.4.

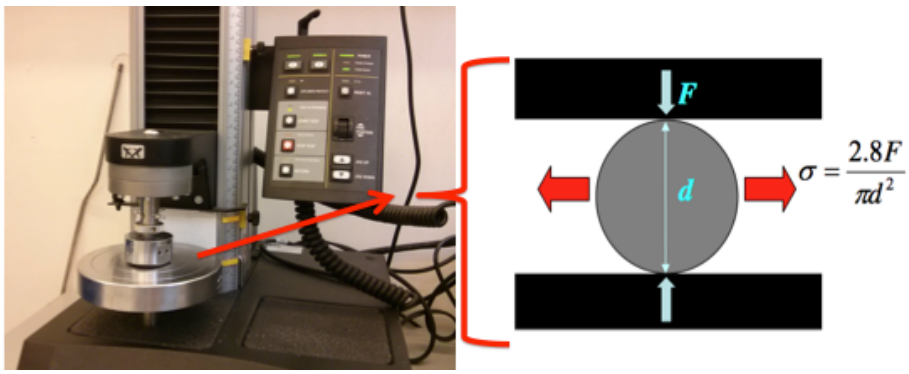

Figure 4.4: *Experimental setup with the Instron 5543 device for uniaxial compression testing. Right illustration shows a sphere placed between load cell platens together with the tensile strength formula.*

Equation first derived by Hiramatsu and Oka [23] that describes the relationship between applied load at break, sphere diameter and tensile strength in brittle spheres under compression was used to approximate tensile strength values for samples.

$$\sigma_{tensile} = \frac{2.8 * F_{break}}{\pi * d^2} \quad [\frac{N}{mm^2}, (MPa)] \qquad \textbf{(4.14)}$$

Equation 4.14: *Hiramatsu & Oka[23], tensile strength of brittle spheres under uniaxial compression.*

4.4.2 Stress distribution

Stress distribution within spheres when load is applied until break was approximated according to Shipway and Hutchings [25] displayed in figure 3.3. The amount of tensile stress distributed along the central axis between loading platens relative to the surface, is dependent on the ratio between the radius of the contact area and the radius of the sphere.

Since deformation of spheres were strictly linear elastic and failure occurs in the elastic zone, the radius of the contact area between platens and spheres a_c, was calculated with Hertzian elasticity solution. The basic Hertzian elasticity solutions for a sphere of radius R at normal load F, are well documented [26]. The radius of the contact area a_c, between sphere and platens with normal load applied until break is given by [28]:

$$a_c = \left(\frac{3}{4} * k * F_{break} * R\right)^{\frac{1}{3}} \qquad \textbf{(4.15)}$$

Where

$$k = \left(\frac{1-\nu_1^2}{E_1} + \frac{1-\nu_2^2}{E_2}\right) \qquad \textbf{(4.16)}$$

Equation 4.15 & 4.16: *Radius of the contact area between sphere and platens at break where (k) is the adjusting constant for different materials.*

E is Young modulus and ν is Poissons`s ratio in eq. 4.16, and the subscript 1 and 2 denotes the particle (sphere) and platen material respectively. The a_c/R ratio was calculated and stressdistribution was derermined graphically using Shipway and Hutchings [25]. Figure 4.5 shows an example of how stress distribution was approximated graphically for sample 1.0/160-12wt%MgO-1150*C, where a_c/R ratio was 0,17.

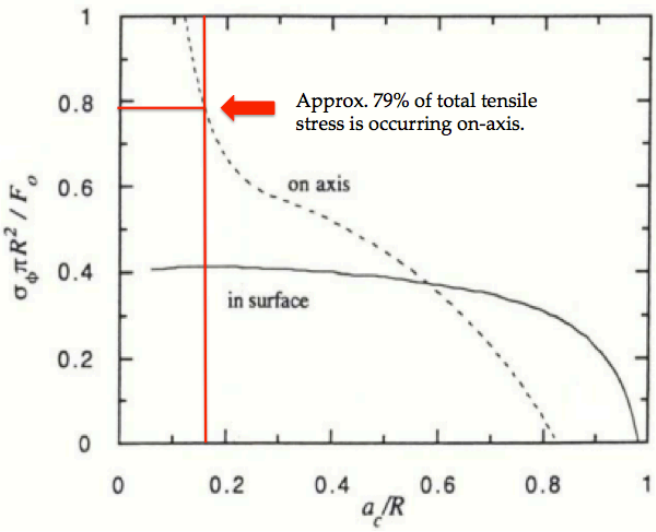

Figure: 4.5: *Graphically usage of Shipway and Hutchings [25].*

Calculations were carried out assuming material properties similar to stainless steel for the load cell, and α-alumina for spheres (table 4.3).

Material	Poisson`s ratio υ	Young's modulus (GPa)
Stainless steel (load cell material)	0.3	193
α- Alumina (sintered)	0.24	380
α- Alumina (sintered) Porosity adjusted (average porosity 0.45)	0.24	≈320

***Table 4.3**: Assumed load cell platen and sample material properties applied in stress distribution approximations.*

4.4.3 Weibull analysis

Weibull analysis provides the advantage in converting full set of material strength data into a failure a probability function, which can easily be used to foresee the failure probability of a specimen at a given stress level. Tensile strength results from each sample were fitted in weibull regression plots to outline differences in tensile strength and reliability for the different sample materials.

Following approach and equations were used to obtain Weibull plots and parameters:

Foundation of calculations is the failure probability function proposed by Weibull (1939) [33]:

$$F(\sigma) = 1 - \exp\left(-\beta_0 * \sigma^m\right) \quad (4.17)$$

***Equation 4.17:** Weibull probability function*

Where σ is the stress at failure, m is the shape parameter (Weibull modulus) and β_0 is the scale parameter. Eq. 4.17 can also be written as a function of normalizing stress, σ_0:

$$F(\sigma) = 1 - \exp\left[-\left(\frac{\sigma}{\sigma_0}\right)^m\right] \quad (4.18)$$

***Equation 4.18:** Weibull function of normalizing stress*

Here σ_0, corresponds to the stress level that gives a failure probability of 63.2%. This stress level is also called the "characteristic strength", and is given by:

$$\sigma_0 = \exp\left(\frac{-ln*\beta_0}{m}\right) \quad (4.19)$$

***Equation 4.19**: Characteristic strength*

Rearranging equation eq. 4.17 and taking the natural logarithm of both sides gives:

$$lnln\left(\frac{1}{1-F(\sigma)}\right) = m * \ln(\sigma) + ln * \beta_0 = m * \ln(\sigma) - m * \ln(\sigma_0) \quad (4.20)$$

Equation 4.20: *Rearranged Weibull probability function*

The Weibull parameters *m and* σ_0 were estimated numerically in Matlab using maximum likelihood estimation functions (MLE). Curve fitting of strength data in accordance to equation 4.20 was also performed in Matlab. The maximum likelihood estimator for parameter σ_0, given *m* is:

$$\sigma_0^m = \frac{1}{N}\sum_{i=1}^{N}(x_i^m - x_N^m) \quad (4.21)$$

Equation 4.21: *MLE for* σ_0 *given m*

Where $x_1 > x_2 > \cdots > x_N$, and N is the largest observed value of specimen in a sample. The maximum likelihood estimator for *m is:*

$$m^{-1} = \left(\frac{\left(\left(\sum_{i=1}^{N}(x_i^m * lnx_i - x_i^m * x_N)\right)\right)}{\left(\sum_{i=1}^{N}(x_i^m - x_N^m)\right)}\right) - \frac{1}{N}\sum_{i=1}^{N} ln\, x_i \quad (4.22)$$

Equation 4.22*: Maximum likelihood estimator for m*

Equation 4.22 is implicit and was solved numerically in Matlab for *m*.

Linear regression analysis can also be used to obtain weibull parameters where an estimator approximates probability:

$$F_i(\sigma) = \left(\frac{i-0.5}{n}\right) \quad (4.23)$$

Equation 4.23: *Probability estimator*

Here *i* is the ranking number of the strength data when ranked in ascending order and *n* is the total number of tested specimens. 33-38 specimens where tested for each sample to provide sufficient amount of data for valid Weibull analysis.

4.4.4 Crush resistance

To evaluate the amount of closure stress proppants (samples) may endure without producing an excess amount of fines, a procedure to determine crush resistance was developed. The suggested crush resistance approximation in this work, is based on Weibull plots, ISO-13502-3 [14], and the relationship between solid strength and crush resistance from Bernhardt`s work on light weight aggregates [28]. This combination results in a quantification of maximum crush resistance, where a given amount of material is crushed.

The crush test from ISO13503-2 [14] says that determination of the highest stress level at which proppants generates no more than 10% crushed material rounded down to the nearest 6.9 MPa (1000 PSI) represents the maximum stress level the material can withstand without exceeding 10% crush. This level will classify the maximum crush resistance for a proppant product.

The relationship between solid strength and crush resistance is given [28]:

$$C \approx \frac{2.8*F_{crit}}{(\pi*d^2)} * \left(\frac{\rho_{bulk}}{\rho_{particle}}\right)^{\frac{2}{3}} = \sigma_{crit} * \eta_{RCP}^{\frac{2}{3}} \qquad (4.24)$$

Equation 4.24: *Crush resistance*

Where σ_{crit} is the critical stress were probability of failure is 10 %, denoted in results as $\sigma_{10\%}$. η_{RCP}, is random close packing of spheres.

The procedure performed for quantifying crush resistance may be described as following:

Weibull probability plot were first established for samples. As an example, figure 4.6 shows the probability plot for the resin-coated proppant. The point on the regression line corresponding to a failure probability of 10% was then found. The accompanying tensile stress level (σ_{crit} *or* $\sigma_{10\%}$) was noted before crush resistance (*C*) was calculated with equation 4.24. To meet the guidelines in ISO-13503-2, calculated values of *C* were rounded down to the closest 6.9 MPa (1000 PSI).

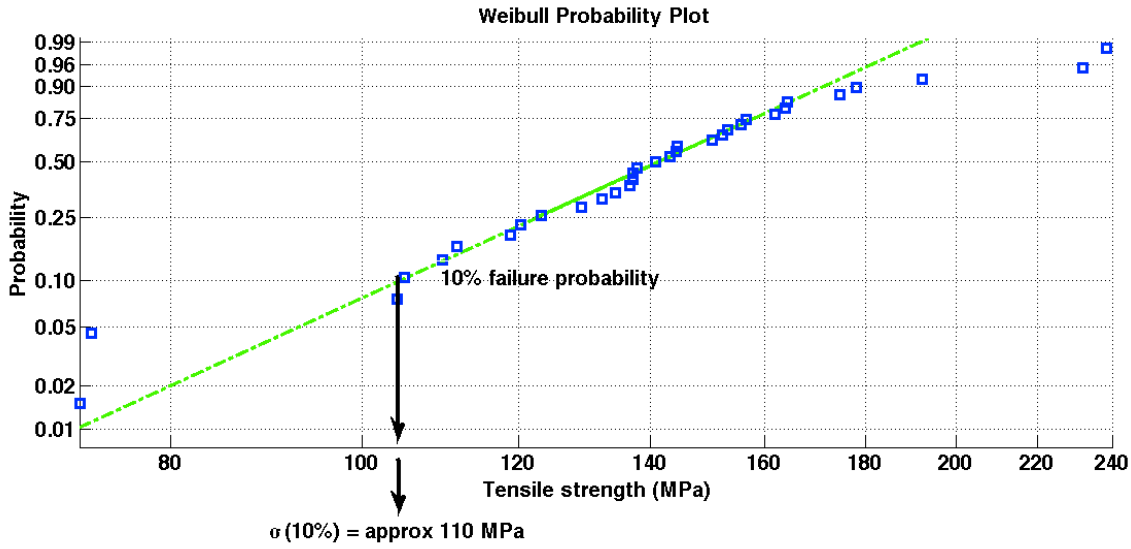

Figure 4.6: *An illustrative example of the Weibull probability plot for the resin coated proppant, and its 10% failure probability level.*

4.4.5 Young's modulus

Young's modulus for samples was based on the average compressive extension and stress level at failure recorded in the uniaxial compression test with the Instron 5543 device. Spherical strain was obtained by dividing the average compressive extension of the piston in Z- direction at break, with average sphere diameter for the current sample. Strain values in this work are consequently a measure of geometrical deformation of spheres, rather than the actual intensive strain of the material.

$$\varepsilon^* = \frac{Average\ compressive\ extension\ in\ z-direction\ (mm)}{average\ sphere\ diameter\ \ (mm)} \qquad \textbf{(4.25)}$$

Equation 4.25*: Geometrical deformation of spheres (Strain)*

$$E = \frac{\sigma_{average}}{\varepsilon^*} \qquad \textbf{(4.26)}$$

Equation 4.26*: E-modulus*

4.5 Characterization

4.5.1 Nitrogen adsorption/ desorption

BET and BJH analysis were performed with a Tristar 3000 Surface area and Porosity Analyser device from Micrometrics. Prior to analysis, all samples were degassed in 250℃ for 24 hours in a VACPREP 061 sample degas system.

4.5.2 X-ray diffraction

XRD measurements/ scans were carried out with a Da Vinci D8 device. 30- minutes scans were performed with 10-75° scanning spectrum and with V6 settings. V6 settings allow the scanned area for a sample to be constant at all scanning angles. A tungsten carbide mortar and pestle were used to grind down alumina spheres to fine powder, before dispersing the powder onto single crystalline quartz sample holders. DIFFRAC EVA 3.0 software was used to characterize and match samples. This software was also used to determined crystallite sizes.

4.5.3 SEM & EDS

Remaining's of crushed sample specimens from the uniaxial compression were collected to investigate fracture surfaces in SEM. Since spheres exploded and little or no remaining's were collectable after a single compression, aluminium foil was used to encapsulate the test environment so that sufficient amount of crushed material could be collected after several compressions. The collected pieces were placed on pin- sample holders using conducting double-sided tape. Two different coating devices were used. Gold was coated in with a Gold Sputter Coater S150B flushed with Aragon gas. Carbon was coated using a Cressington Carbon Coater. AZtec software was used in EDS- analysis.

5 Main results

5.1 Physical & geometrical properties

Tables below show an overview of basic physical and geometrical properties for samples prior and post treatment. Table 5.1 display properties for the 1.0 mm diameter sphere samples. Table 5.2 is the equivalent information for the 1.8 mm diameter spheres but also including properties for the commercial resin coated proppant.

Average diameter is measured from 30-35 different spheres. Theoretical density is calculated from the nominal composition of alumina and magnesium oxide, and the crystallographic densities are recorded in XRD. Particle density is the density of each sphere. Paricle porosity is the porosity within each sphere. Bulk density includes the particle density, particle porosity and the matrix porosity. Bulk density is the product of particle density and random close packing.

Sample type 1.0/160	Average diameter, D_{30}**[mm]**	Theoretical density, $\boldsymbol{\rho_{Teoretical}}$ $[\boldsymbol{g/cm^3}]$	Particle density, $\boldsymbol{\rho_{particle}}$ $[\boldsymbol{g/cm^3}]$	Particle porosity, $\boldsymbol{\phi}$	Bulk density, $\boldsymbol{\rho_{Bulk}}$ $[\boldsymbol{g/cm^3}]$	Random close packing $\boldsymbol{\eta_{RCP}}$
Base material $\boldsymbol{\gamma - Al_2O_3}$	1.110	3.66	1.34	0.64	0.73	0.55
Base material-1150℃ $\boldsymbol{\alpha - Al_2O_3}$	0.860	4.05	2.72	0.33	1.49	0.55
5wt% MgO-1000℃	1.020	3.65	1.70	0.53	0.92	0.54
5wt% MgO-1100℃	0.840	3.97	2.89	0.27	1.56	0.54
5wt% MgO-1150℃	0.830	3.97	3.13	0.21	1.72	0.55
12wt% MgO-1000℃	1.050	3.64	1.65	0.57	0.85	0.52
12wt% MgO-1060℃	0.99	3.86	1.97	0.48	1.11	0.56
12wt% MgO-1150℃	0.866	3.85	2.94	0.24	1.37	0.54
15wt% MgO-1140℃ (USI)	0.826	3.81	3.47	0.09	1.90	0.55
15wt% MgO-1150℃ (USI)	0,821	3.81	3.54	0.07	1.95	0.55

Table 5.1: *Sasol alumina spheres. Initial sphere size: 1,0 mm. Prior and after IWI, USI with Mg- nitrate and calcinations.*

Figure 5.1 below illustrates how particle density and porosity are varying with increasing calcination temperature for the 1.0 diameter spheres. Main observations are densification, porosity drop and noticeable differences between samples prepared with 5 and 12- wt% MgO. Densification is most significant when the $\gamma \rightarrow \alpha$ phase transition is reached, above 1000℃.

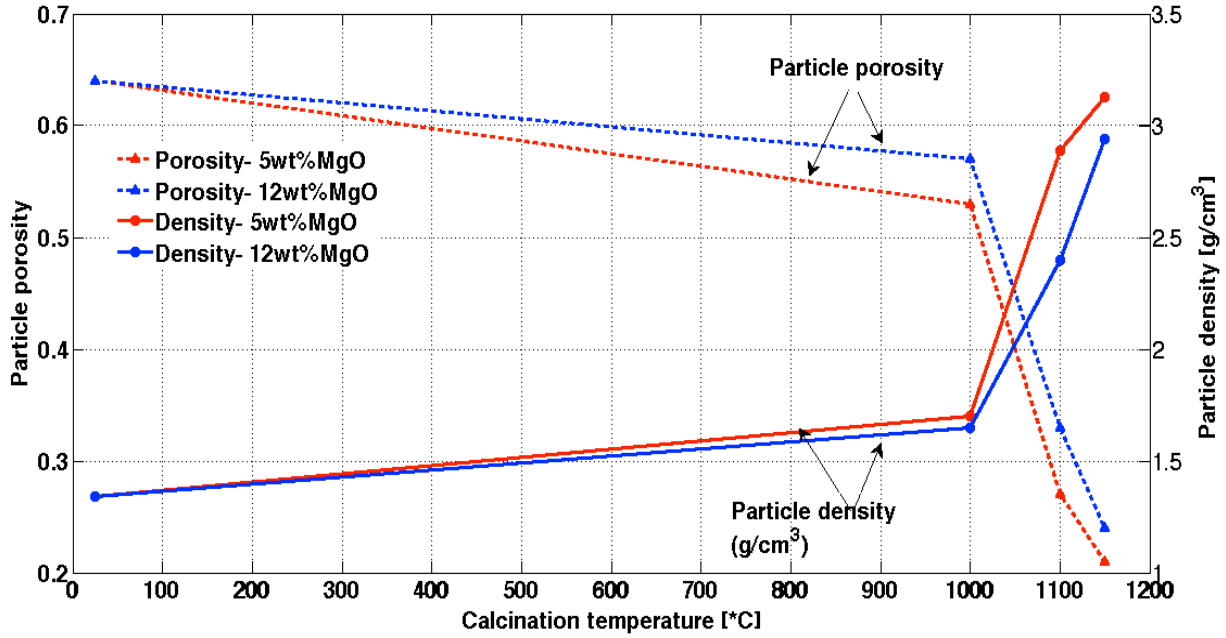

Figure 5.1: *Densification and porosity drop increasing with calcination temperature for 1.0 mm-size samples prepared with 5- and 12wt% MgO (IWI). "Dashed" lines: Porosity (left Y-axis).*

Similar development with densification and porosity loss post calcination is also observed for 1.8 size samples. The difference between 5 and 13 wt.% MgO content is however less evident for the 1.8 size samples.

Sample 1.8 & RCP	Average diameter, D_{30} **[mm]**	Theoretical density, $\boldsymbol{\rho_{Teoretical}}$ $[\boldsymbol{g/cm^3}]$	Particle density, $\boldsymbol{\rho_{particle}}$ $[\boldsymbol{g/cm^3}]$	Particle porosity, $\boldsymbol{\phi}$	Bulk density, $\boldsymbol{\rho_{Bulk}}$ $[\boldsymbol{g/cm^3}]$	Random close packing $\boldsymbol{\eta_{RCP}}$
Base material $\gamma - Al_2O_3$	1.72	3.66	0.97	0.73	0.52	0.54
Base material-1150℃ $\alpha - Al_2O_3$	1.35	4.05	1.87	0.53	1.05	0.56
5wt% MgO-1100℃	1.32	3.97	2.18	0.45	1.18	0.54
5wt% MgO-1125℃	1.31	3.97	2.23	0.44	1.23	0.55
5wt% MgO-1150℃	1.28	3.97	2.33	0.41	1.28	0.55
Resin coated proppant (RCP)	1.08	-	2.72	-	1.56	0.57
13wt% MgO-1000℃	1.66	3.64	1.35	0.62	0.76	0.56
13wt% MgO-1150℃	1.31	3.85	2.33	0.40	1.35	0.58

Table 5.2: *Commercial resin coated proppant & Sasol alumina spheres with initial sphere size: 1,8 mm. Prior and after IWI with Mg- nitrate and calcination.*

Worth noticing from table 5.1 and 5.2 is that total densification percentage prior and after calcination is higher for 1.8 spheres than for 1.0 spheres. Densification is also higher for samples containing [MgO], than for the non- impregnated base material post calcination treatments.

5.1.1 Permeability dependent properties

As described in theory, roundness, sphereicity and narrow size distribution of proppant particles is important for optimal permeability. Table 5.3 below gives a comparison of permeability related properties for the Sasol alumina spheres 1.8 and 1.0 and the resin coated proppant product investigated. High $\boldsymbol{\eta_{RCP}}$ values are associated with broad size distribution and therby reduced matrix porosity.

Sample	Roundness	Sphereicity, Φ_s	Average random close packing, $\boldsymbol{\eta_{RCP}}$	Matrix porosity, ϕ_M
Sasol alumina spheres 1.0	>0.95	>0.95	0.545	0.455
Sasol alumina spheres 1.8	>0.95	>0.95	0.56	0.44
Resin coated proppant (RCP)	0.9	0.9	0.57	0.43

Table 5.3: *Comparison of conductivity dependent properties for Sasol alumina spheres 1.0, 1.8 & the resin- coated proppant.*

5.2 Mechanical properties

High mechanical integrity is essential for functional proppants. The results from the investigation of mechanical properties are presented in this section. Weibull analysis provides most central observation regarding mechanical behaviour and microstructural character. Crush resistance results are also important to evaluate if samples inhibit sufficient mechanical strength to be applied as proppants in unconventional reservoirs.

5.2.1 Stress distribution & failure mechanism

Approximations based on Shipway and Hutchings relationship[25] described in experimental reveals that approx. 80% of the total stresses at brake occurs along the central axis of sample spheres, perpendicular to the uniaxial load applied. It is therefore reasonable to assume that the alumina spheres at scope, fails due to tensile stresses that arises along the central axis. SEM pictures of fracture surfaces also support this assumption *(Figure 5.2)*.

Catastrophic failure mechanism is generally observed. Spheres explode at failure and little or nothing of the remains is collectible afterwards. This was especially the case for smaller diameter spheres.

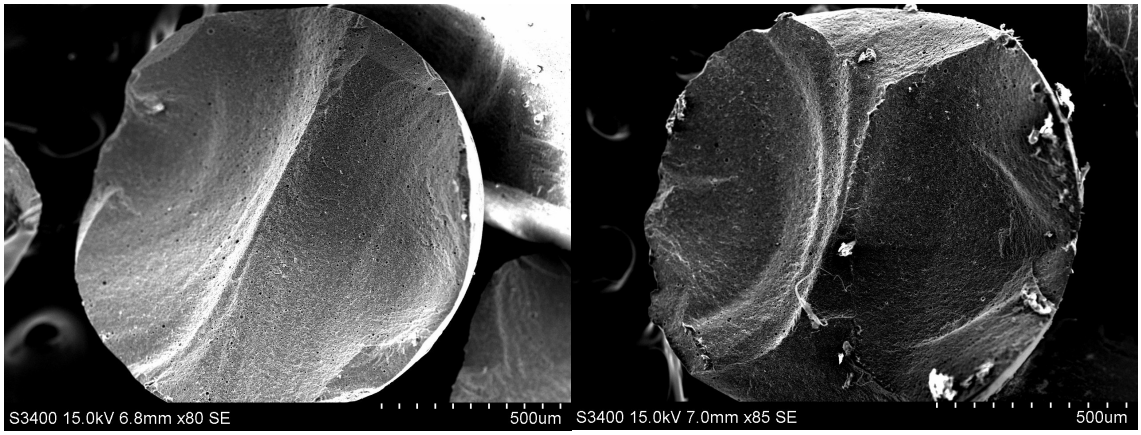

Figure 5.2: *SEM photos of two different fracture surfaces from sample 1.8-13wt%MgO-1150, illustrating tensile stresses perpendicular to the central axis that have torn the spheres apart, when a uniaxial compressive load was applied.*

5.2.2 Weibull tensile strength analysis

Uniaxial compression results are converted to Weibull probability functions in in this section. Figures below present plots for a selection of specimen samples. All plots in this section are displayed in log-log scale, where the X- axis represents the measured tensile strength at break (MPa), and Y-axis the corresponding failure probability. Data for calculated characteristic strength (σ_t) and Weibull modulus (m) for each sample is given in the figures. This data is also summerized in *table 5.4* in section 5.2.3 along with other related data.

Figure 5.3 below show comparisons of base material for 1.8 and 1.0 mm sized spheres prior and post calcination at 1150℃ (γ to α- alumina). Main observations are an increase in tensile strength and decrease in Weibull modulus (m) from γ to α- phase. It is also evident that smaller diameter spheres yield higher tensile stress values and lower reliability values (m). Weakest link theory supports this observation [34].

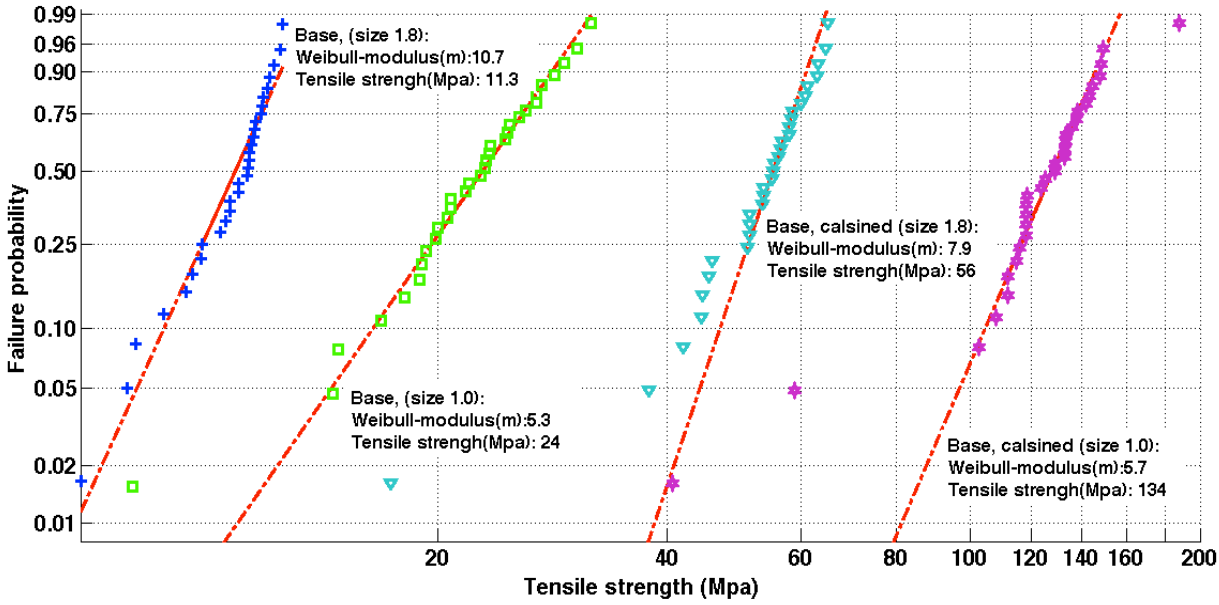

Figure 5.3: *A comparison of base material for 1.8 and 1.0 sized spheres prior and post calcination at 1150*℃.

Figure 5.4 shows probability plots for 1.8 mm sized spheres prepared with incipient wetness impregnation (IWI), containing 5wt% MgO, calcined at 1100, 1125 and 1150℃. An increase in characteristic tensile strength, and a decrease in Weibull modulus (m) are observed with increasing calcination temperature.

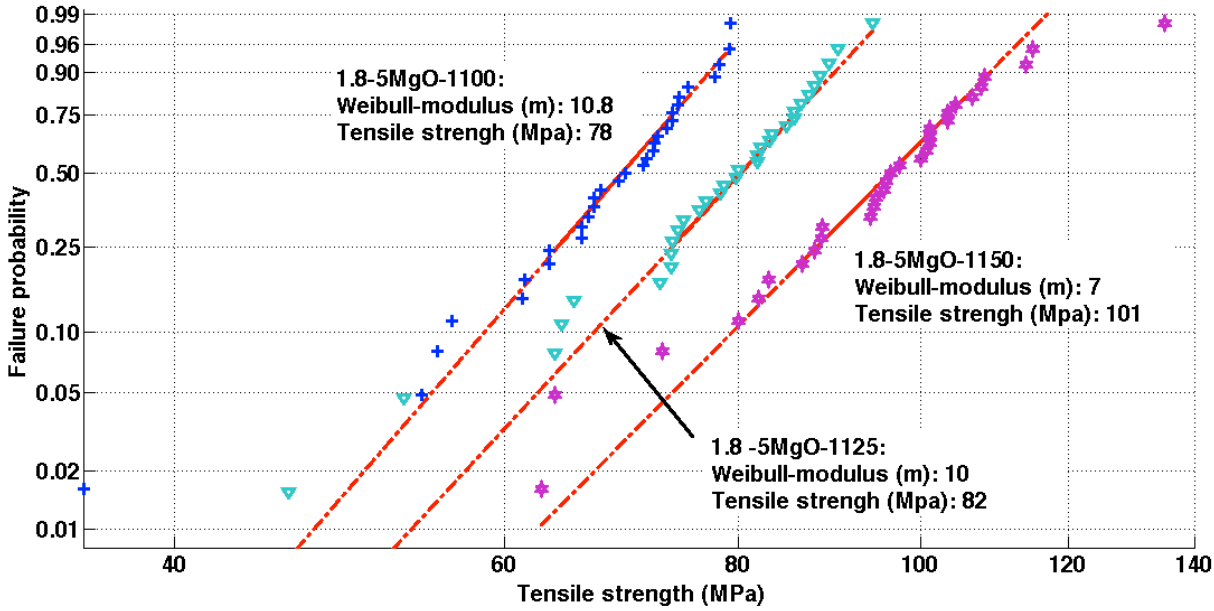

Figure 5.4: *Weibull probability plots for 1.8 sized specimens, containing 5wt% MgO, prepared with IWI and calcined at 1100, 1125 & 1150*℃.

Figure 5.5 shows plots for 1.0 mm sized spheres, IWI-prepared and containing 5wt% MgO. Calcination temperatures: 1000, 1100 and 1150℃. Increase in calsination temperature leads to an increase in characteristic tensile strength. Spheres calsined at 1100℃ display noticeable lower reliability (*m*) than samples calcined at 1000 and 1150℃. Highest reliability (*m*) is observed for specimens' calcined at 1150℃.

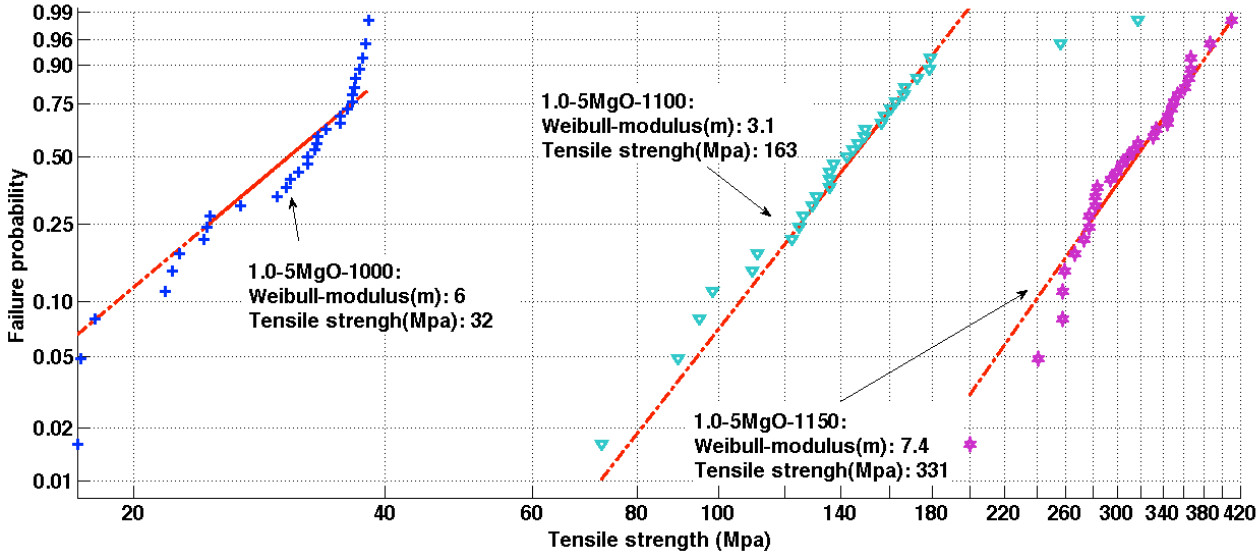

Figure 5.5: *Weibull probability plot for 1.0 mm sized spheres, IWI- prepared, containing 5wt% MgO, calcined at 1000, 1100 & 1150*℃.

Figure 5.6 compares 1.8 and 1.0 mm- sized spheres containing 13 and 12 wt.% MgO (IWI), calcined at 1000 and 1150°C. This figure illustrates the difference in mechanical properties between 1.8 and 1.0 mm sized spheres containing similar wt.% of MgO. Significant strength increase is observed for both sphere sizes from calcination at 1000°C to 1150°C. The reliability (*m*) of the data is increasing from 3.8 to 5.3 for the 1.8 mm sized sample while decreasing from 5.7 to 3.3 for 1.0 mm sized samples between the two calcination temperatures. In general, lower weibull modulus (*m)* is observed for IWI- samples with higher wt.% MgO. Higher tensile strength- values are obtained for low MgO- content for the 1.0 mm sized specimens, while high MgO- content yields highest strength values for 1.8 mm sized specimens. This relationship is only observed for incipient wetness impregnated samples.

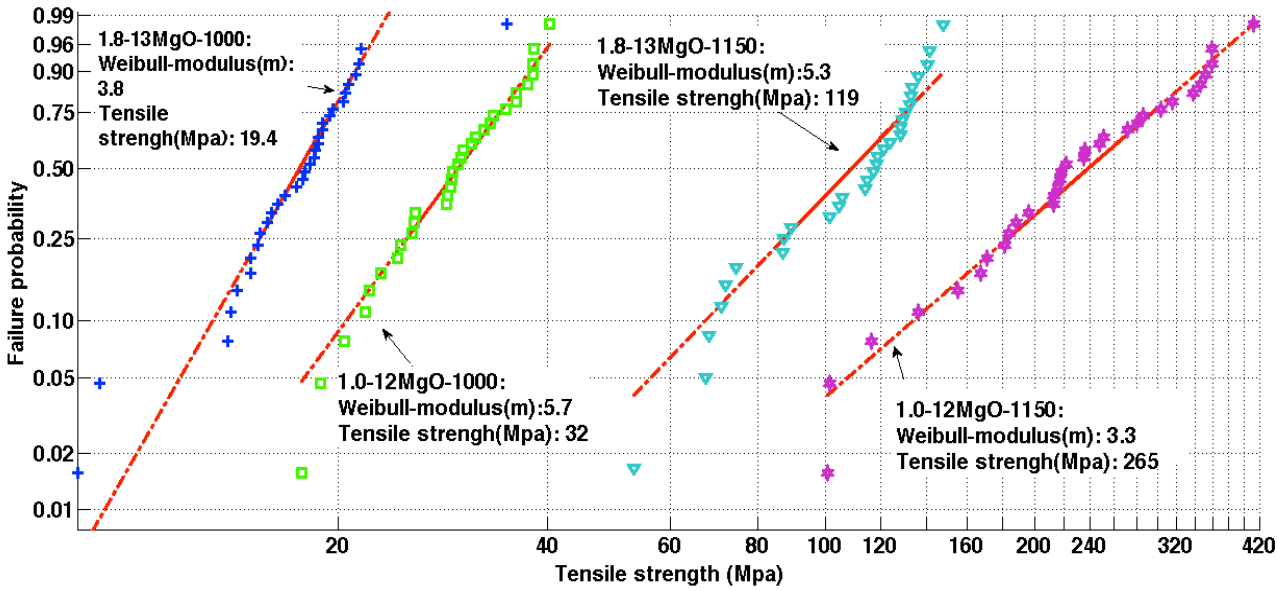

Figure 5.6: *Comparison of 1.8 and 1.0 mm sized spheres, prepared with 13 and 12wt% MgO (IWI), and calcined at 1000 and 1150* °C.

Samples that displayed high mechanical strength are compared with a commercial resin coated proppant product (RCP) in figure 5.7. This figure also illustrates the significant improvement in mechanical properties obtained when ultrasonic impregnation (USI) are included in the sample preparation. From the two 1.0 -15wt% MgO (USI) samples, it is also evident that mechanical properties are improved with calcination treatment at 1140℃ compared with 1150℃. Values for both weibull modulus (m), and characteristic tensile strength (σ_T) were obseerved higher when calcination is performed at 1140℃.

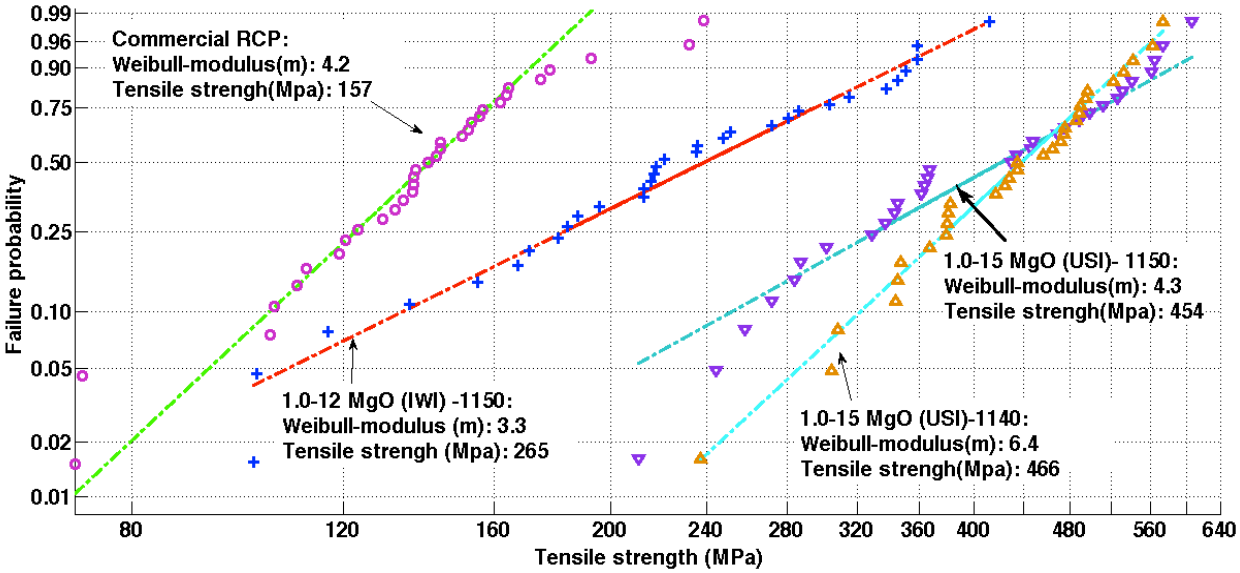

Figure 5.7: *Comparison of samples with high mechanical performance, and the commercial RCP product. Figure also illustrates differences in mechanical properties for samples prepared with IWI and USI, along with improved properties for samples calcined at 1140℃ rather than 1150℃.*

5.2.3 Crush resistance

Crush resistance approximation according to ISO-13503-2 and Bernhardt [28] are displayed in table 5.4 below. Parameters form the Weibull analysis is also included in this table. Figure 5.8 gives an overlook of crush resistance for samples as a function of calcination temperature.

Sample:	Weibull modulus, m	Characteristic tensile strength, σ_T [Mpa]	Stress at 10% failure probability, $\sigma_{10\%}$ [MPa]	Crush resistance, C (rounded*) [PSI, (MPa)]
1.0-Base (**γ-alumina**)	6.3	24	18	1000 (6.7)
1.0-Base (**α-alumina**)	5.7	134	105	10 000 (69.0)
1.0-5wt% MgO-1000℃	6	32	19	1000 (6.7)
1.0-5wt% MgO-1100℃	3.1	163	109	10 000 (69.0)
1.0-5wt% MgO-1150℃	7.4	331	240	**23 000** (158.6)
1.0-12wt% MgO-1000℃	5.7	32	21	2000 (13.8)
1.0-12wt% MgO-1150℃	3.3	265	139	**13 000** (90.0)
1.0-15wt%MgO-1140℃ (USI)	**6.4**	466	320	**30 000** (207.0)
1.0-15wt%MgO-1150℃ (USI)	**4.3**	454	250	24 000 (166.0)
Resin coated proppant (RCP)	4.2	157	110	**10 000** (69.0)
1.8-Base (γ-alumina)	10.7	11,3	5	0 (0)
1.8-Base (α-alumina)	7.9	56	48	4000 (27.6)
1.8-5wt%MgO-1100℃	10.7	78	59	5000 (34.5)
1.8-5wt%MgO-1125℃	**10**	82	68	6000 (41.4)
1.8-5wt%MgO-1150℃	7	101	80	7000 (48.3)
1.8-13wt%MgO-1000℃	3.8	19,4	9,5	0 (0)
1.8-13wt%MgO-1150℃	5.3	119	68	5000 (34.5)

Table 5.4: *Summary of parameters form Weibull analysis. Crush resistance approximated according to ISO-13502-2 [14] and Bernhardt et al. 2013[28].*

Both weibull modulus (m), and calculated characteristic tensile strength (σ_T) affect the approximated crush resistance. High values of weibull modulus means that the regression line fitted with the test data becomes steeper and thereby decreases the probability of 10% crushed material at a given stress. Difference between samples 1.0- 12wt% and 1.0 -5wt% calcined at 1150°C illustrates the imprortance of weibull modulus when crush resistance are regarded. While the characteristic tensile strength of the 5wt%- sample is just about 25% higher than for the 12wt% sample, the crushing resistance becomes 77% higher due to higher weibull modulus value found for the 5wt% sample.

Highest crush resistance is recorded for the 1.0-15wt% ultrasonic impregnated sample, where highest weibull modulus and characteristic tensile strength is observed after calcination at 1140°C. As mentioned, theres a clear difference in crush resistance between the 1.0- 5wt% and 1.0-12wt% samples. For the 1.8-5wt% and 1.8-13wt% samples, the difference in crush resistance is not as evident. In both sphere sizes prepared with incipent wetness impregnation, the crush resistance and Weibull modulus is higher for lower MgO content (5wt%).

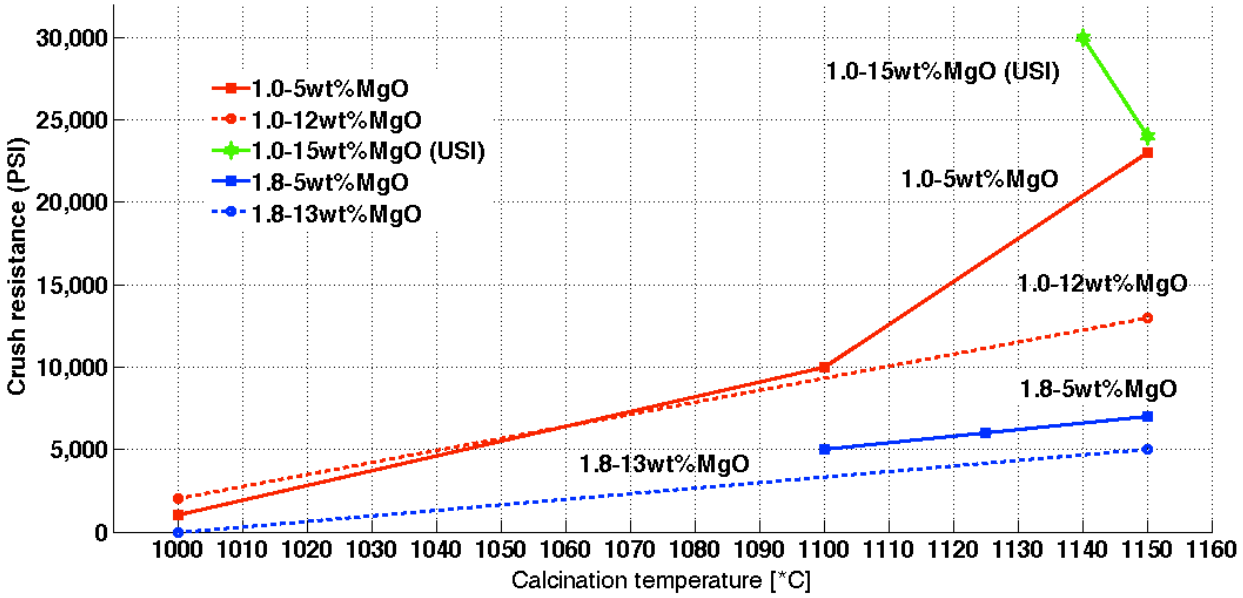

Figure 5.8: *Crush resistance as a function of calcination temperature for 1.8 & 1.0 mm sized spheres with different MgO- content (wt.%) and impregnation method.*

5.2.4 E- modulus *

E-modulus plots for 1.0 mm sized samples and the resin-coated proppants are presented in figure 5.9 below. X-axis represents the average tensile stress at break for each sample. Y-axis represents average deformation (displacement) over the average diameter of test specimens. Figure 5.10 show equivalent plots for 1.8 mm sized spheres.

Ps. Values for strain in these two figures is a quantification of spherical deformation, not true strain. Therefore, "E- modulus"- values are essentially the stiffness of the body, which is an extensive property, and not the real E-modulus, which is an intensive material property.

Highest average tensile stress and spherical deformation ("strain") at break is observed for the ultrasonic prepared specimens. However, highest stiffness is observed for the 12wt% MgO sample calcined at 1150°C. For IWI- prepared samples stiffness (E-modulus*) seems to be increasing with increasing wt% MgO content for calcination temperatures at 1150°C. Stiffness is also increasing with increasing calcination temperature. An interesting observation is that higher stiffness is found for the IWI prepared sample with 12wt% MgO than for the ultrasonic prepared sample that inhibits greater density. This is a contradiction regarding theory [19].

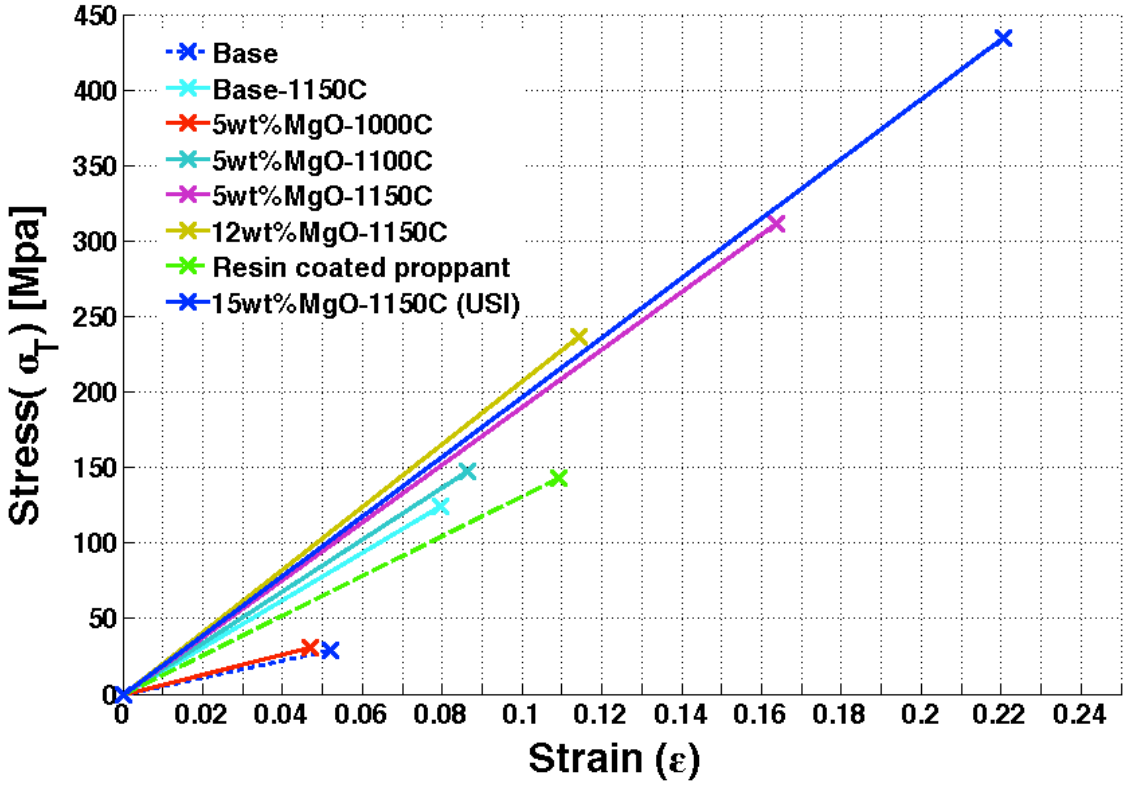

Figure 5.9: *Stress & strain plots for 1.0-mm sized spheres and RCP. Varying MgO- content and calcination temperatures.*

The same trends for stiffness are observed for the 1.8 mm spheres (Fig.5.9). Highest stiffness (E-modulus*) is found for 13wt% MgO- specimens calcined at 1150°C. Differences between the two specimen sizes may however be observed. 1.8 mm spheres prepared with 13wt% MgO can endure higher stress and strain before failure than its counterpart containing 5wt% MgO. The opposite relationship is found for 1.0 mm specimens.

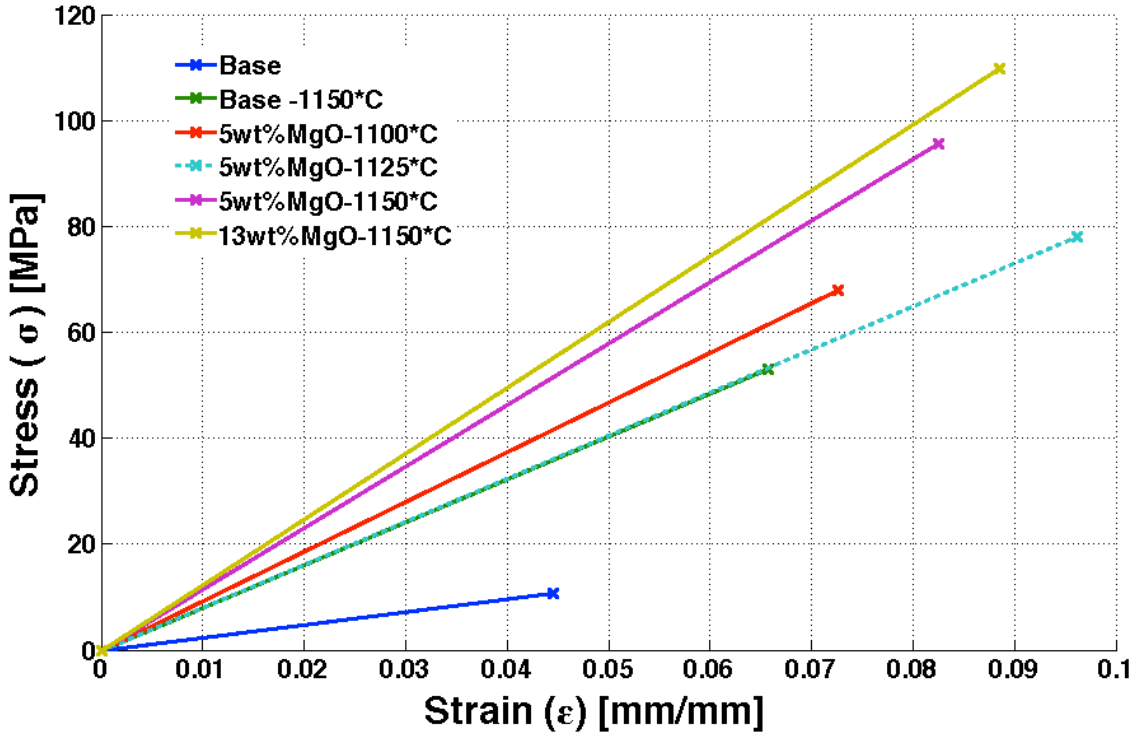

Figure 5.10: *Stress & strain plots for 1.8 mm-sized spheres. Varying MgO- content and calcination temperature.*

5.3 N_2- Adsorption /Desorption

This section shows results on how surface area and pore volume of samples varies with impregnated amount of MgO and calcination temperature. Current result is relevant to evaluate the possibility of multi- functional proppants using the material under investigation, and to observe trends in order to further improve these properties.

5.3.1 BET Surface area

Figure 5.11 show how BET surface area is varying with calcination temperature for 1.0 and 1.8 - *mm* specimens prepared with 5, 12,13 and 15wt% MgO. Sample prepared with ultrasonic aid is also included in this figure (light green cross). It is evident that all samples undergo large drops in BET surface area with increasing calcination temperature. This drop is most significant when calcination temperatures surpasses 1000℃ and into the $\gamma \rightarrow \alpha$ –phase trasition region. The base material (γ- alumina) 1.0 and 1.8 starts out with BET surface area of approx. 160 m^2/g and 210 m^2/g respectively. After calcination at 1000℃, surface area declines to approx. 100 m^2/g for both 1.0 and 1.8- mm sized spheres that were prepared with 12 & 13wt% MgO. For 1.0- mm specimens impregnated with 5wt% MgO surface area is sustained higher (118 m^2/g) after calsination at 1000℃.

After calcination at 1150℃, the highest sustained surface area is 18.5 m^2/g and observed for the 1.0- mm specimens prepared with 12 wt%MgO.

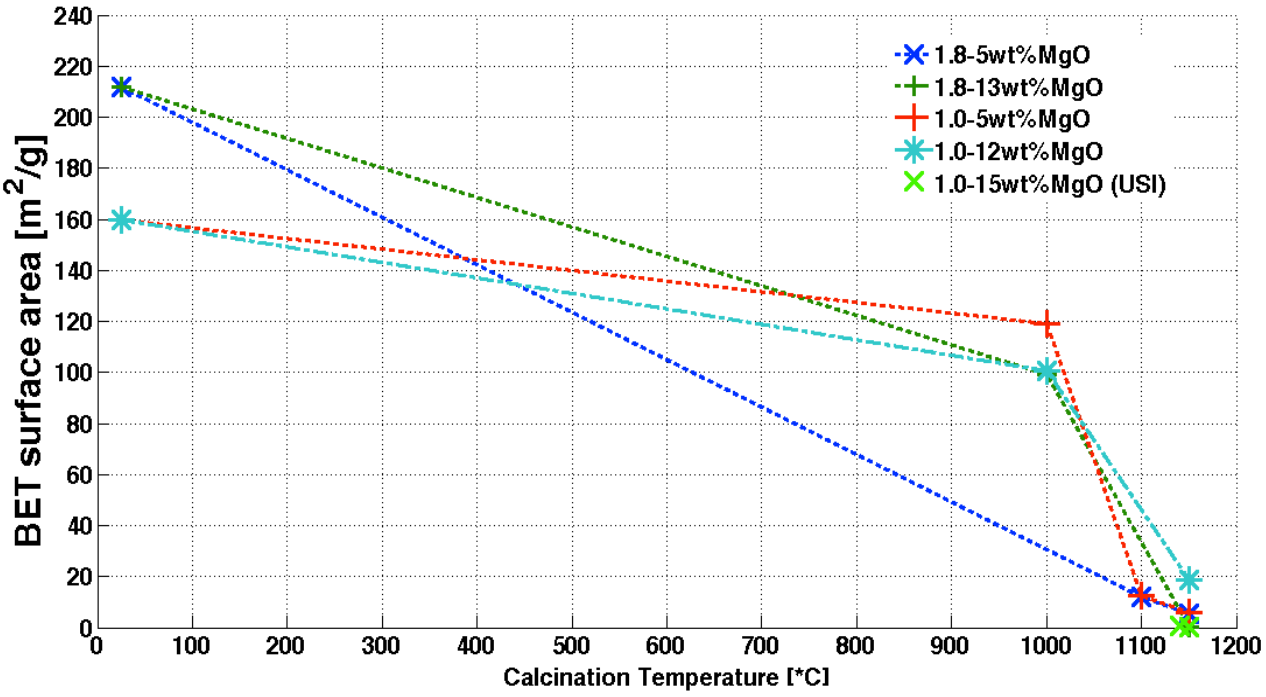

Figure 5.11: *BET surface area as a function of calcination temperature for 1.0 and 1.8 mm sized samples prepared with 5, 12& 13wt% MgO.*

Figure 5.12 below displays the change in BET surface area as a function of wt.% MgO- content for 1.0 and 1.8 –mm specimens calcined at 1150°C. While surface area decrease with increasing MgO- content for 1.8 mm specimens, the opposite relation is observed for 1.0 - mm specimens.

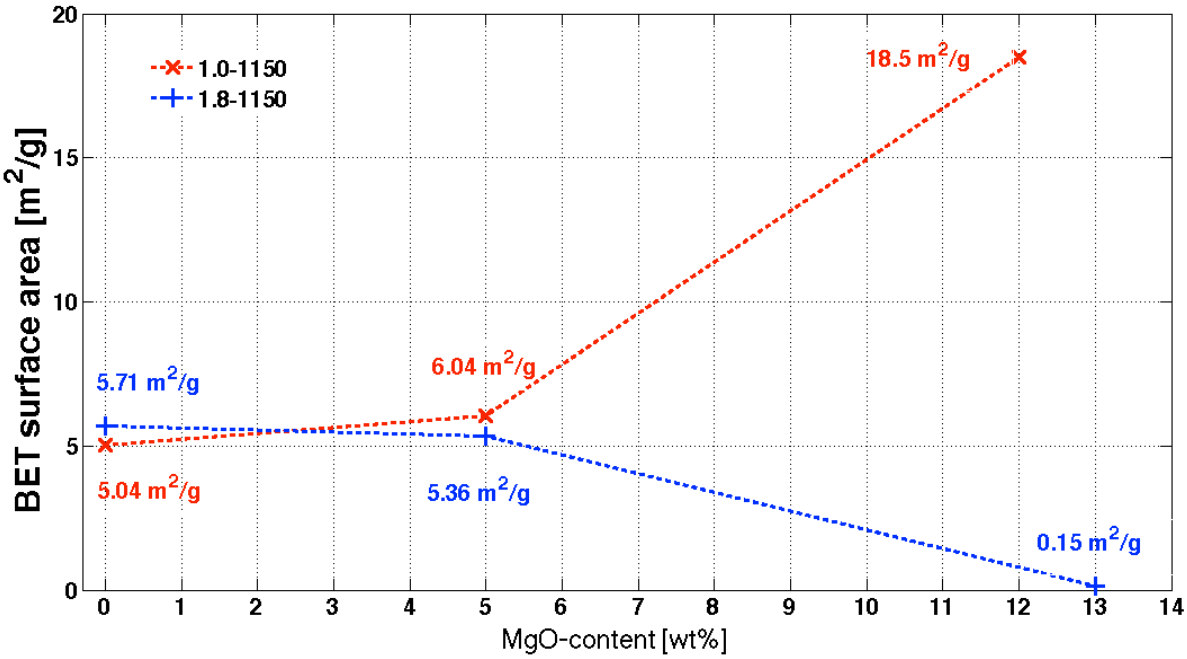

Figure 5.12: *BET surface area as a function of wt.% MgO for 1.0 & 1.8 mm sized spheres for constant calcination temperature (1150°C).*

BHJ pore volume was also plotted for all samples that is displayed in figure 5.11, and can be found in appendix. BJH pore volume as a function of wt.% MgO at 1150 °C (similar to figure 5.12) can also be found in appendix. The same trends that are observed for BET surface area dependent on calcination temperature and MgO content, is generally also evident for BJH pore volume.

5.3.2 Pore area & pore volume size- distribution

Pore area and pore volume- size distribution is displayed in this section. The goal for this investigation is to determine size distribution of pores for specimens at scope. This information is useful to explain the variations in properties observed after modification treatments for different sample specimens.

Pore volume distribution is displayed in figure 5.13 for 1.0 and 1.8 mm sized γ- alumina (Base material) and 12-13wt% MgO- content. Pore volume is distributed over pore diameters with peaks at approx. 12.5-13 nm for 1.0 base spheres, and approx. 10 nm for 1.8 base spheres. The peak is evidently sharper for the base material 1.0- mm sample than for the 1.8- sample. Pore volume is more narrowly distributed around the sharp peak. Pore volume distribution shifts slightly after impregnation and calcination at 1000℃ for both size samples, and distribution curves are more similar with peaks around 13-14 nm. The 1.0 mm sphere still display higher pore volume after treatment.

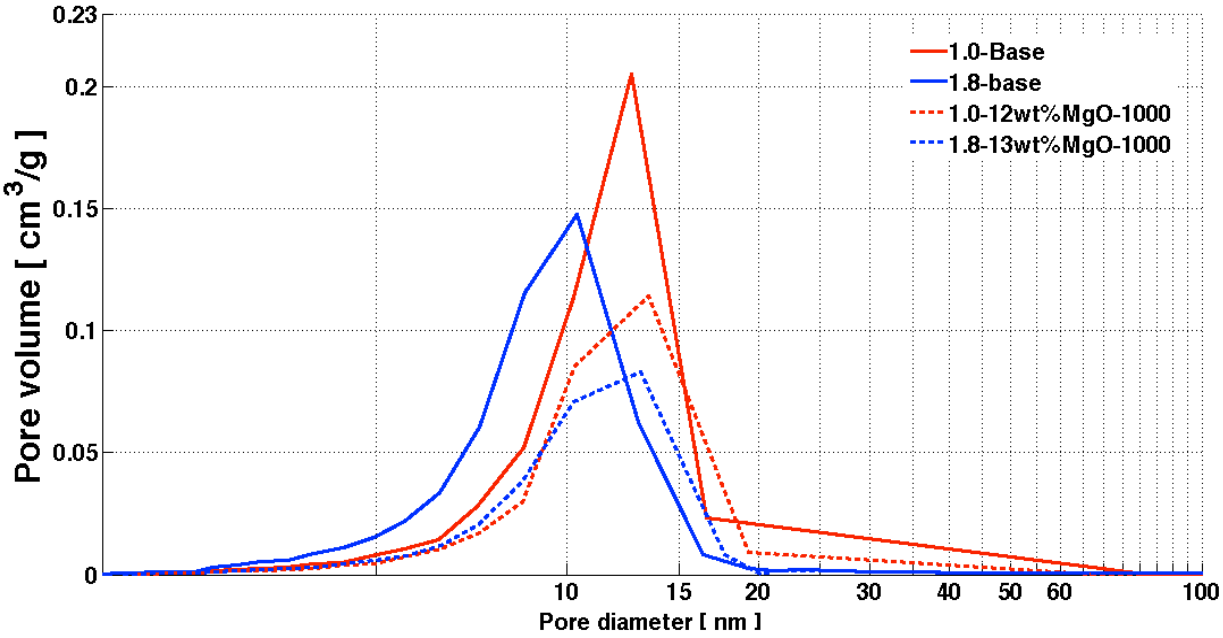

Figure 5.13: *BJH- dV /log(D) - pore volume. Average pore size distribution of pore volume for gamma alumina base material, 1.0 and 1.8 mm size spheres. Dashed lines represent the base material calcined at 1000℃.*

In figure 5.14, pore area distribution over pore diameters is plotted for the exact same samples that are displayed in figure 5.13. Curves are also similar in character, but the 1.8- mm sample display higher pore area values. Peaks for pore area are approximately at similar positions as for pore volume. Shape of the distribution is also similar for both base and treated sample materials.

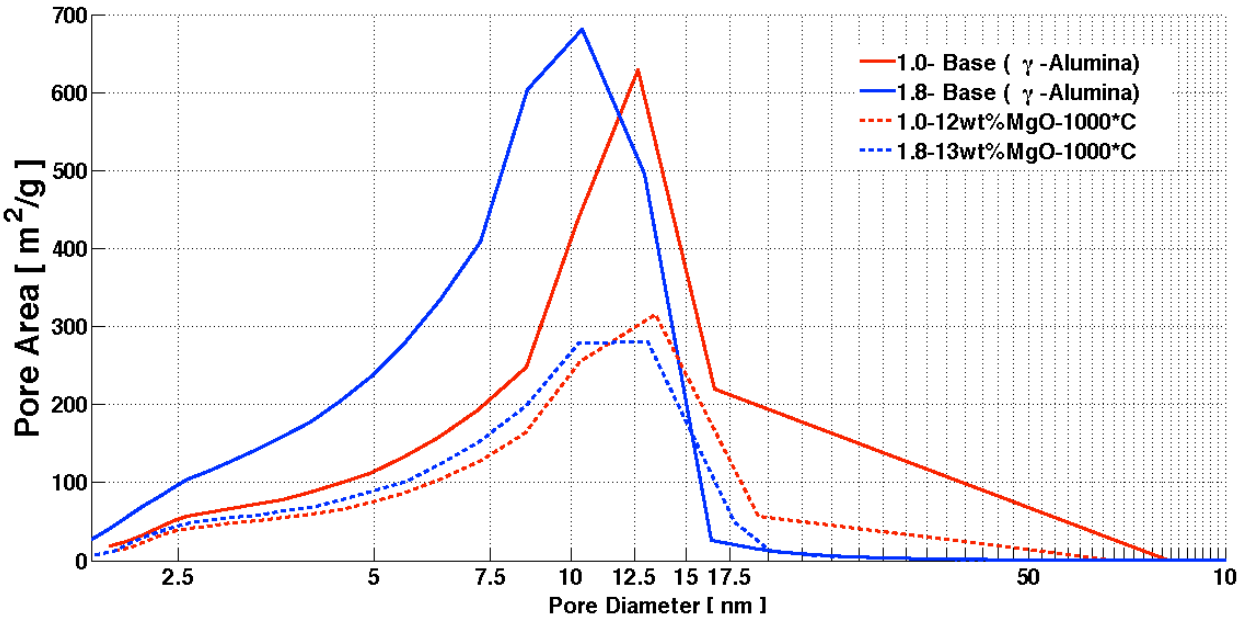

Figure 5.14: *Pore area distributed over pore diameter. 1.0 and 1.8 mm sized spheres, base material and 12-13 wt% MgO content (dashed lines)*

To outline changes, pore volume and pore area distribution is also plotted for impregnated samples that were calcined at 1150°C. Figure 5.15 show pore volume distribution over pore diameters for both 1.0 and 1.8 mm sized specimens after the treatment mentioned above. Both specimen sizes containing 5wt% MgO display that pores in the region of 3-20 nm almost completely closes after calcination at high temperature. This is not the case for the 1.0-12wt% MgO sample where some pore volume remains for pore diameter peak around 11-14 nm.

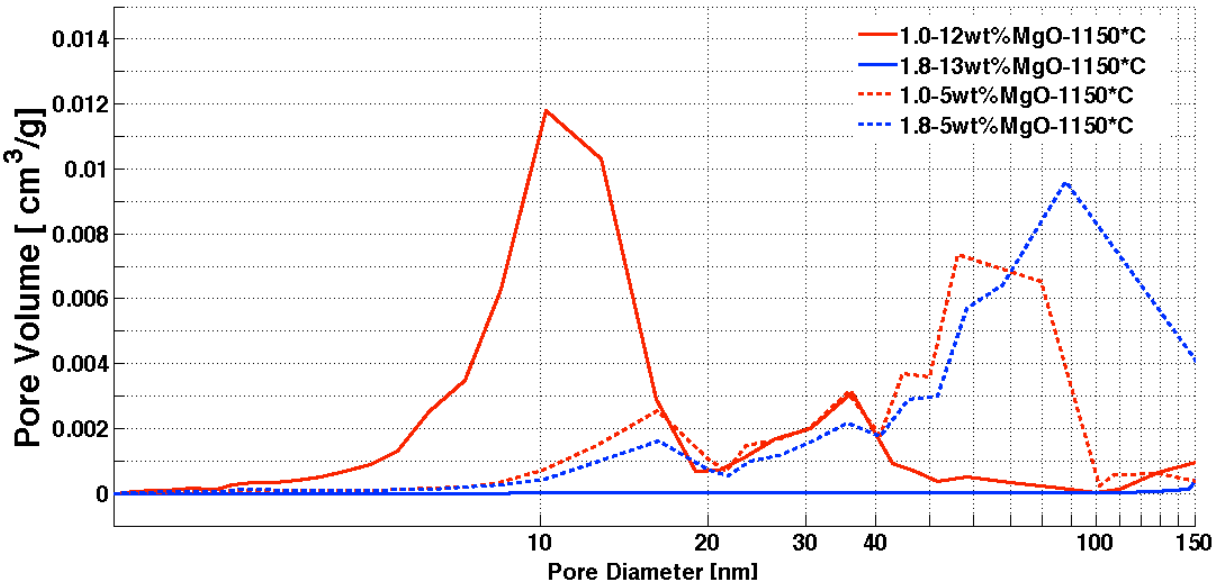

Figure: 5.15*: BJH Adsorption dV/d*log(D) Pore volume. Pore volume distributed over pore diameter for 1.0 and 1.8 mm spheres, IWI (5 &12-13 wt.% MgO), calcination: 1150°C.*

Figure 5.16 show area of pores distributed over pore diameters for the same samples as in fig.5.15. The area of pores more or less disappears for all samples after high temperature calcination, except for the 1.0 mm spheres containing 12 wt.% MgO, that retains some pore area with a peak around 10-12.5 nm.

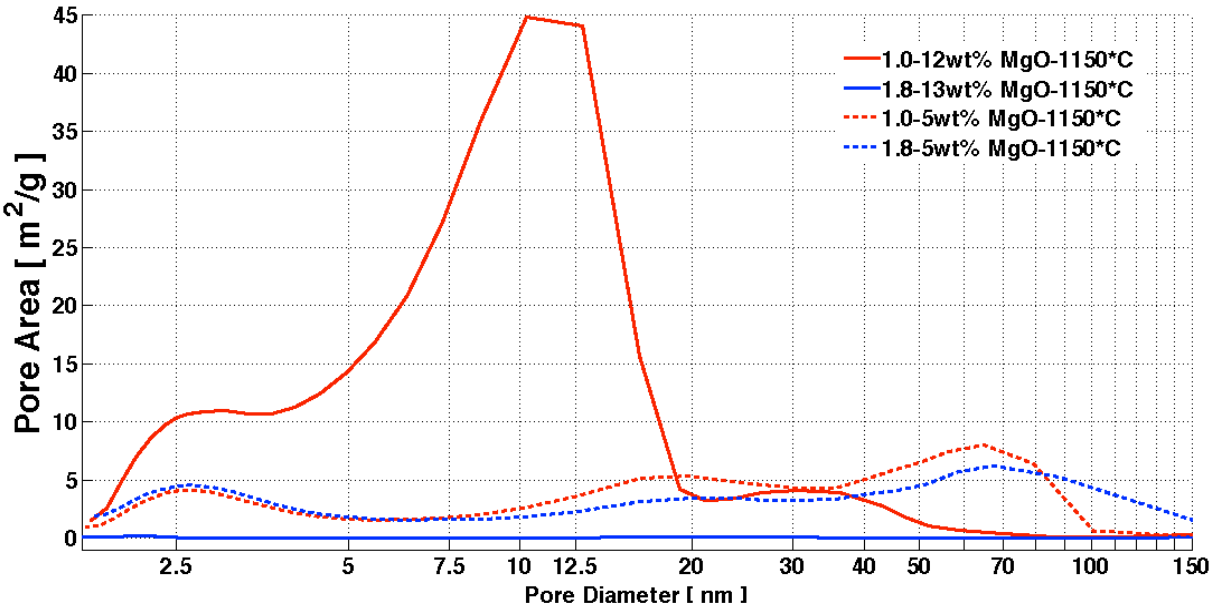

Figure: 5.16: *Pore area distributed over pore diameter for 1.0 &1.8 mm spheres, IWI (5 &12-13wt% MgO), Calcination: 1150*℃.

Plots for pore volume and pore area distribution of α- alumina samples are provided in the appendix.

5.4 Open /Closed particle porosity

Even though BJH- pore volume measurements did provide reasonable trends for changes depending on calcination and impregnation treatments (Appendix), values obtained did not accurately describe the open pore volume in absolute terms for samples examined separately. Therefore ultrasonic aided water absorption was carried out to investigate the actual open pore volume that is accessible with a fluid.

Results from pore volume measurements performed with *ultrasonic water absorption* are presented in figure 5.17, where total and open porosity are plotted as a function of calcination temperature. Dashed lines represent the total porosity at the left y-axis, and volume% ***of the total porosity*** is at the right y-axis. The total porosity started at 0.64 for 1.0 mm spheres and 0.73 for 1.8 mm spheres. The total porosity decreased with increasing temperatures and most significant decreased occurred when calcination temperatures surpassed 1000°C, as earlier pointed out.

The most interesting observation for this measurement is that; while vol% of open porosity decreases along with total porosity drop for 1.8 specimens, the vol% of open porosity for the 1.0 specimen impregnated with similar amount of MgO, remains almost completely intact.

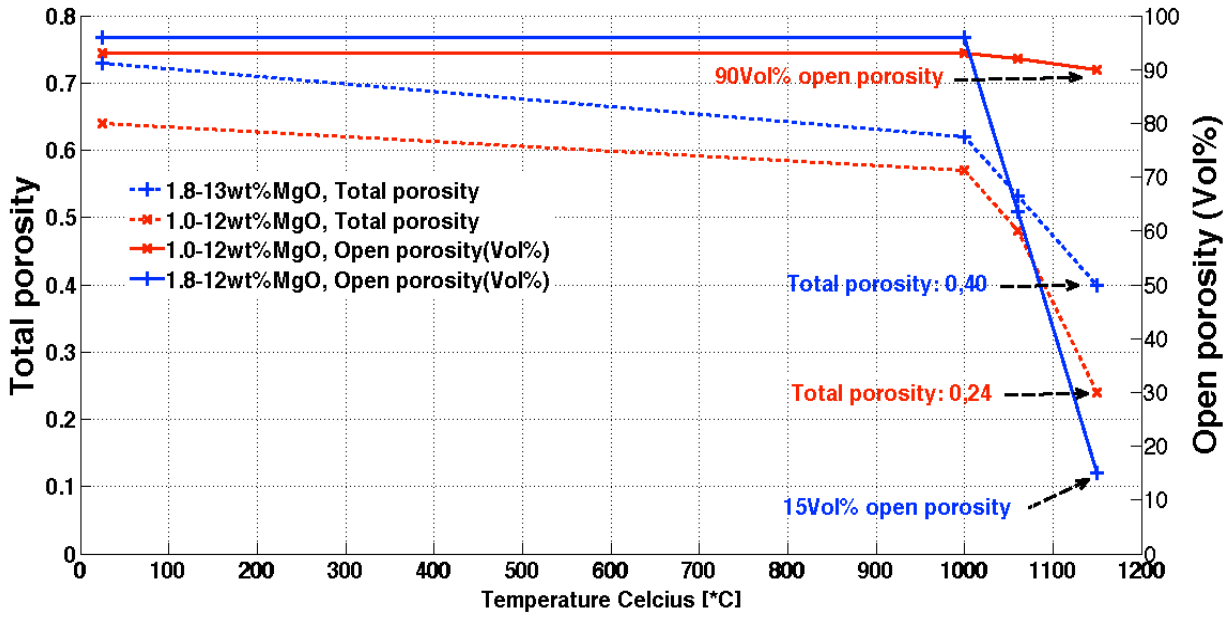

Figure 5.17: *Total and open porosity as a function of calcination temperature. 1.8 & 1.0 mm sphere sizes. IWI-prepared with 12-13 wt.% MgO.*

5.5 X-ray diffraction

In figure 5.18, XRD- scans are displayed for high temperature calcined base material (α- alumina) and IWI- samples containing 12 and 13 wt.% MgO for 1.0 and 1.8 mm spheres.

This figure outlines the different impact impregnation treatment inflicts on different sphere sizes. While the base material for 1.0 and 1.8 mm spheres show identical scans after high temperature calcination, distinct differences are observed for the same sized specimens after impregnation with similar concentrations. Most obvious is the broad spinel peak recorded for the impregnated - 1.0 spheres relative to the impregnated 1.8- spheres. Another clear observation is the differences spinel peak location observed for the impregnated samples after high temperature calcination. Also a higher intensity for the spinel peak relative to the α- alumina is noticed for 1.0 spheres compared with 1.8 spheres. α- Alumina peaks are also sharper and with higher intensity for the impregnated 1.8 spheres, relative to 1.0 spheres with equivalent treatment.

Ps. Eta denotes magnesium alumina- spinel phase in figures.

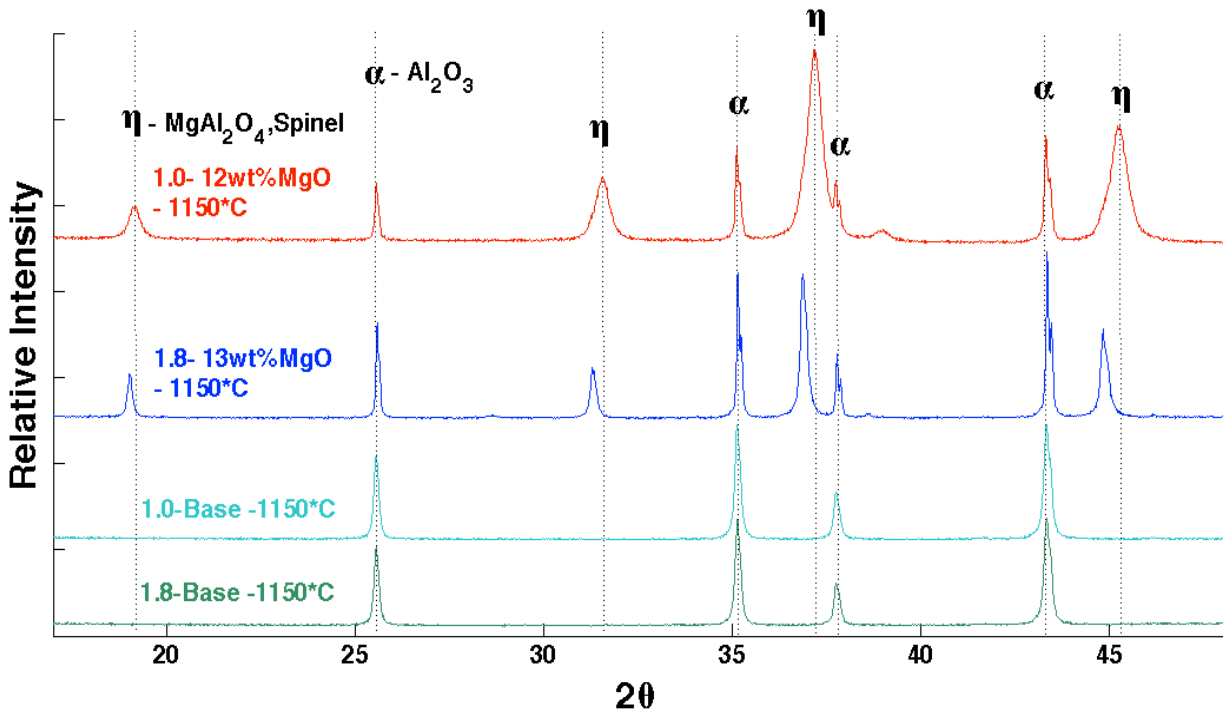

Figure 5.18: *α-alumina & α-alumina+ spinel (ss) identified for 1.0 and 1.8 mm sized spheres. Figure outlines the different impact impregnation inflicts for 1.0 and 1.8 mm spheres.*

Figure 5.19 show XRD scans recorded for 1.8 mm samples, prior and post impregnation and calcination with varying MgO -content and temperature treatments. Figure provide information about how phases evolve with temperature and MgO- content. The widths of the peaks for both spinel and α- alumina are slightly decreasing from 1100 -1150°C for samples prepared with 5wt% MgO. Intensity increases with increasing temperature for the same samples. Intensity for α-alumina peaks for impregnated samples is generally higher than for the base material when both are calcined at 1150°C. α- Alumina peaks are also sligntly broader for samples without impregnation treatment. Evident diffrences between 5 and 13wt% MgO- content are noted. Intensity of the spinel peak is increasing with increased MgO content, simultaneously as α-alumina peaks decrease. Sharper peaks are observed for higher MgO contents for 1.8 mm spheres.

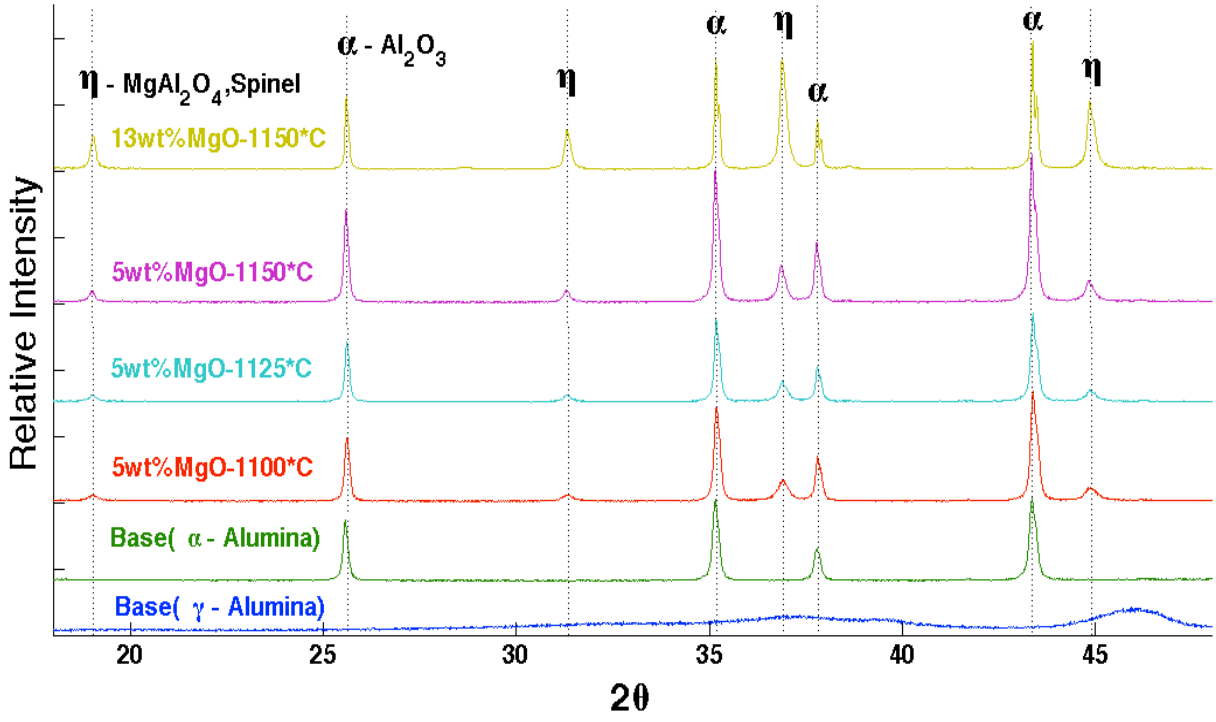

Figure 5.19: *XRD scans for 1.8 mm spheres prior and post impregnation and calcination. Figure outlines phase evolvement for 1.8 mm samples.*

In figure 5.20, scans from 1.0-sized spheres containing different MgO content prepared with USI and IWI and calcined at 1140- 1150°C are plotted and compared. The difference between the two ultrasonic prepared samples with 15wt% MgO is not clear, but still observable. Sample calcined at 1140°C shows slightly broader spinel peaks. The main observation in this figure is the clear difference in spinel peaks between samples prepared with IWI compared to USI. The 12wt% MgO sample shows higher spinel intensity relative to α- alumina compare to other samples. Its spinel peaks are alsosignificanly broader and shiftthed to he left as erlier pointed out. As also displayed in figure 5.19 for 1.8 mm spheres, the relative intensity of spinel peaks are increasing with increasing MgO content.

In this figure; highest tensile strength and crush resistance is found for the USI prepared sample containing 15wt% MgO and calcined at 1140°C, while highest stiffness (E-modulus), BET surface area, and open porosity is found for the sample containing 12wt% MgO calcined at 1150°C.

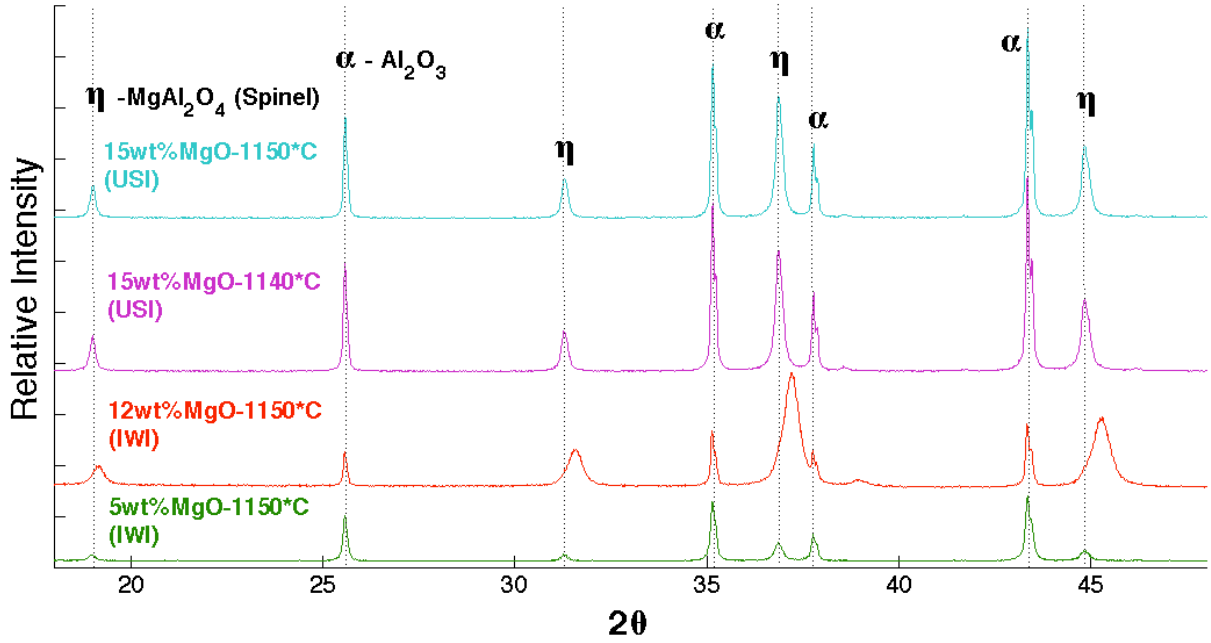

Figure 5.20: *1.0 spheres containing 5, 12, and 15wt% MgO, prepared with IWI and USI and calcined between 1140 and 1150°C.*

Crystallite sizes are approximated for all samples in figure 5.18-20, and are given in table 5.5 in the next section.

5.5.1 Crystallite size

Crystallite sizes for samples in section 4.5 (XRD plots) are shown in table 5.5. Note that crystallite- size values are approximated with "Diffrac.Suite 3.0"- software and are not absolutely accurate for samples evaluated separately. Data is however useful to observe changes depending on variables such as MgO - content, calcination temperature or preparation methods.

Sample		**Crystallite size**	
Sphere size (mm)	Wt.%[MgO]- Calcination temp. (℃) (Impregnation method)	$\boldsymbol{MgAl_2O_4 - spinel}$ (nm)	$\boldsymbol{\alpha - Al_2O_3}$ (nm)
1.0	Base-1150℃	**-**	**66**
1.0	5-1150℃ (IWI)	**52**	**90**
1.0	12-1150℃ (IWI)	**21**	**105**
1.0	15-1140℃ (USI)	**57**	**121**
1.0	15-1150℃ (USI)	**65**	**122**
1.8	Base-1150	-	**70**
1.8	5-1100℃ (IWI)	**38**	**72**
1.8	5-1125℃ (IWI)	**45**	**83**
1.8	5-1150℃ (IWI)	**59**	**83**
1.8	13-1150℃ (IWI)	**73**	**129**

Table 5.5: *Approximation of crystallite sizes for the spinel and α-phase.*

5.6 SEM & EDS

Sample: 1.8 mm γ- alumina (Base material untreated).

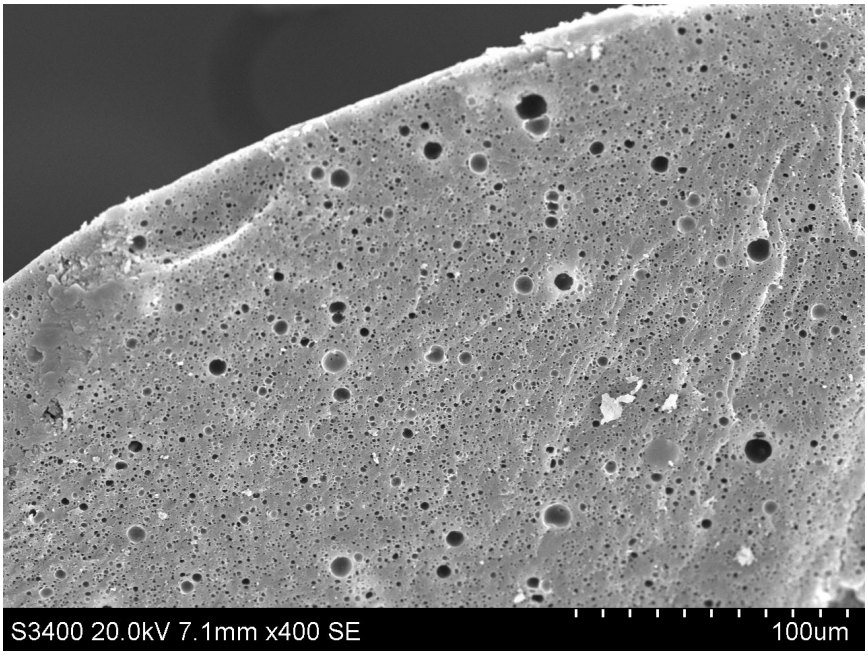

Figure 5.21: *An overview photo. Fracture surface. Magnification x400. Fracture surface. γ- Alumina sphere. Untreated. Measurement scale: 100μm. Accelatration voltage: 20 kV.*

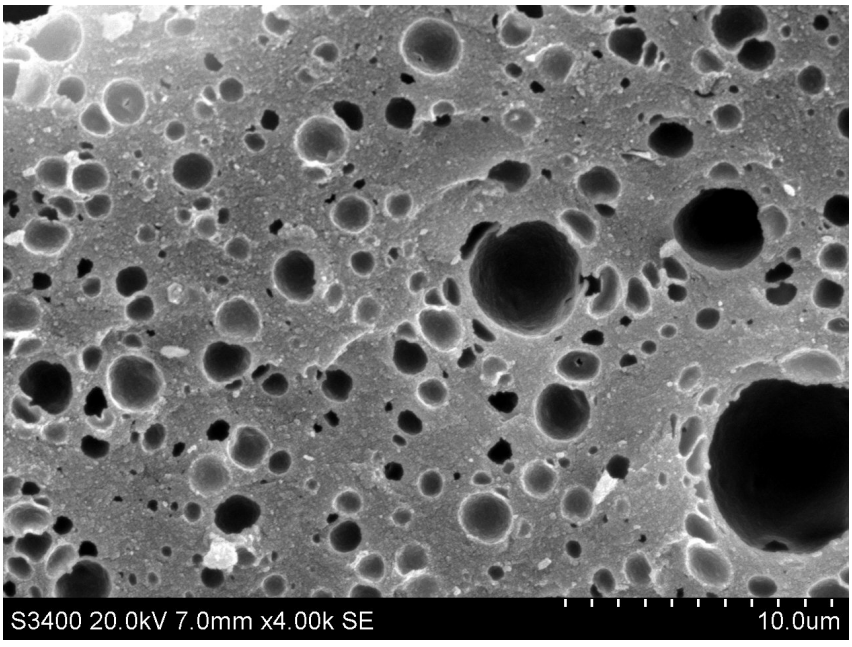

Figure 5.22: *Close-up. Fracture surface. Magnification x 4.0 k. γ- Alumina sphere. Untreated. Measurement scale: 10μm. Accelatration voltage: 20 kV.*

Sample: 1.8 α -Alumina (Base material calcined at 1150℃)

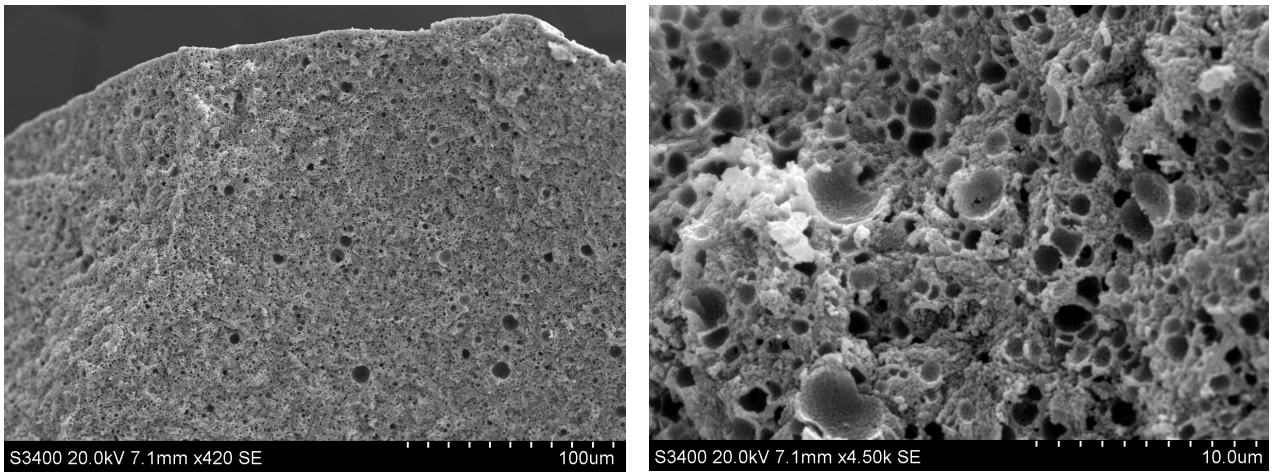

***Figure 5.23 (Left photo)**: An overview. Fracture surface. Magnification: x420. α –Alumina. Measurement scale: 100µm. Acceleration voltage: 20 kV.*

***Figure 5.24 (Right photo)**: Close-up. Fracture surface. Magnification: x4.5 k. α –Alumina. Measurement scale: 10µm. Acceleration voltage: 20 kV.*

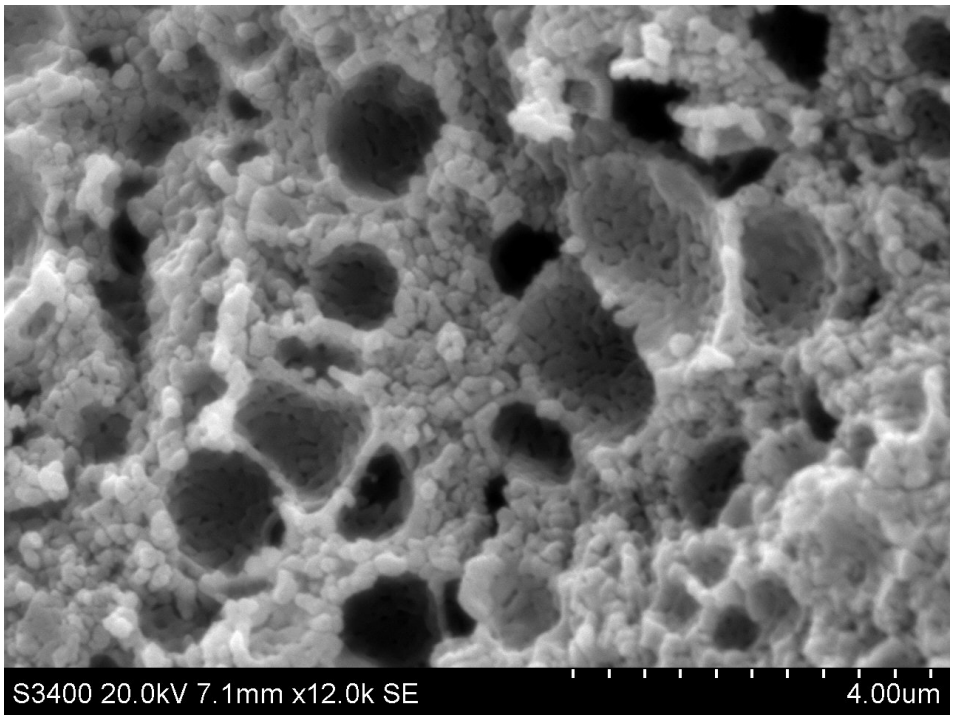

***Figure 5.25:** High magnification: x12 k. Fracture surface. α –Alumina. Measurement scale: 4µm. Acceleration voltage: 20 kV.*

Sample: 1.8 mm -5wt%MgO- 1150℃

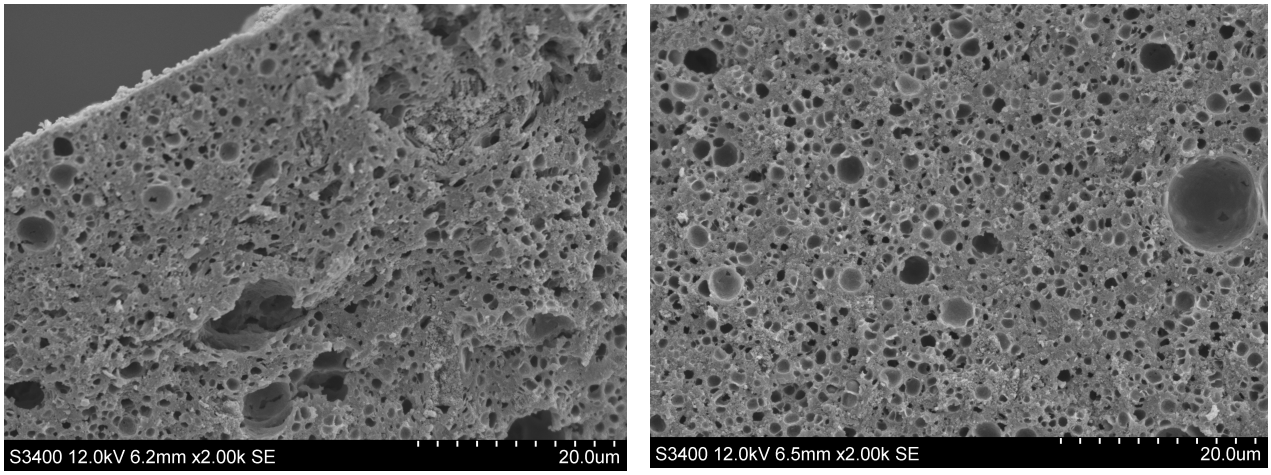

***Figure 5.26 (Left photo)**: Fracture surface. Specimen edge. Magnification: x 2.0k. 5wt% MgO (IWI). Calcination temperature: 1150℃. Measurement scale: 20µm. Acceleration voltage: 12 kV.*

***Figure 5.27 (Right photo)**: Fracture surface. Specimen centre. Magnification: x 2.0k. 5wt%-MgO (IWI). Calcination temperature: 1150℃. Measurement scale: 20µm. Acceleration voltage: 12 kV.*

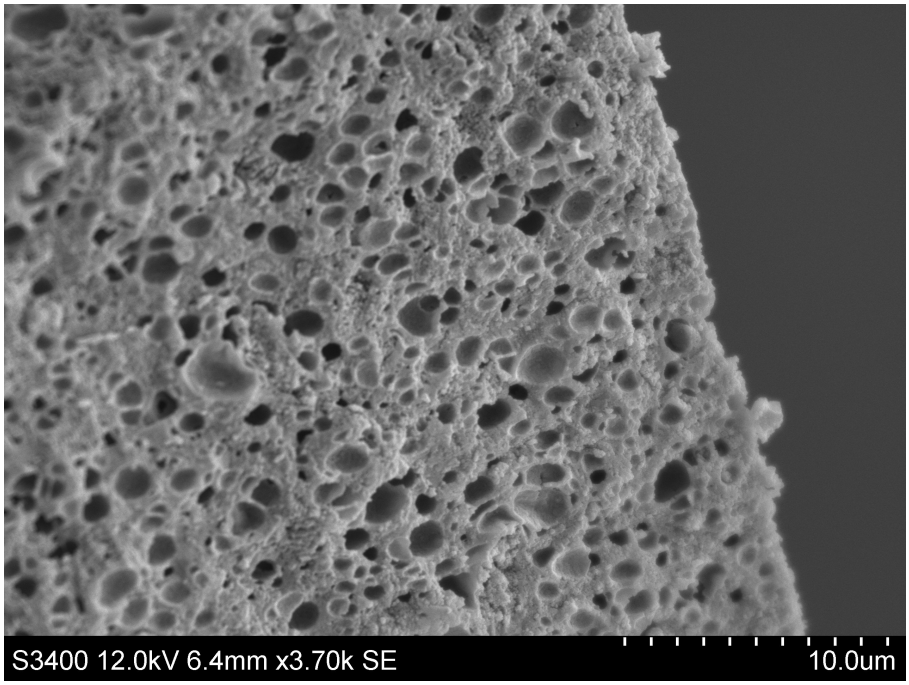

***Figure 5.28:** Fracture surface. Specimen edge. Magnification: x 3.7 k. 5wt% MgO (IWI). Calcination temperature: 1150℃. Measurement scale: 20µm. Acceleration voltage: 12 kV.*

EDS

Sample: 1.8 mm -5wt%MgO- 1150℃

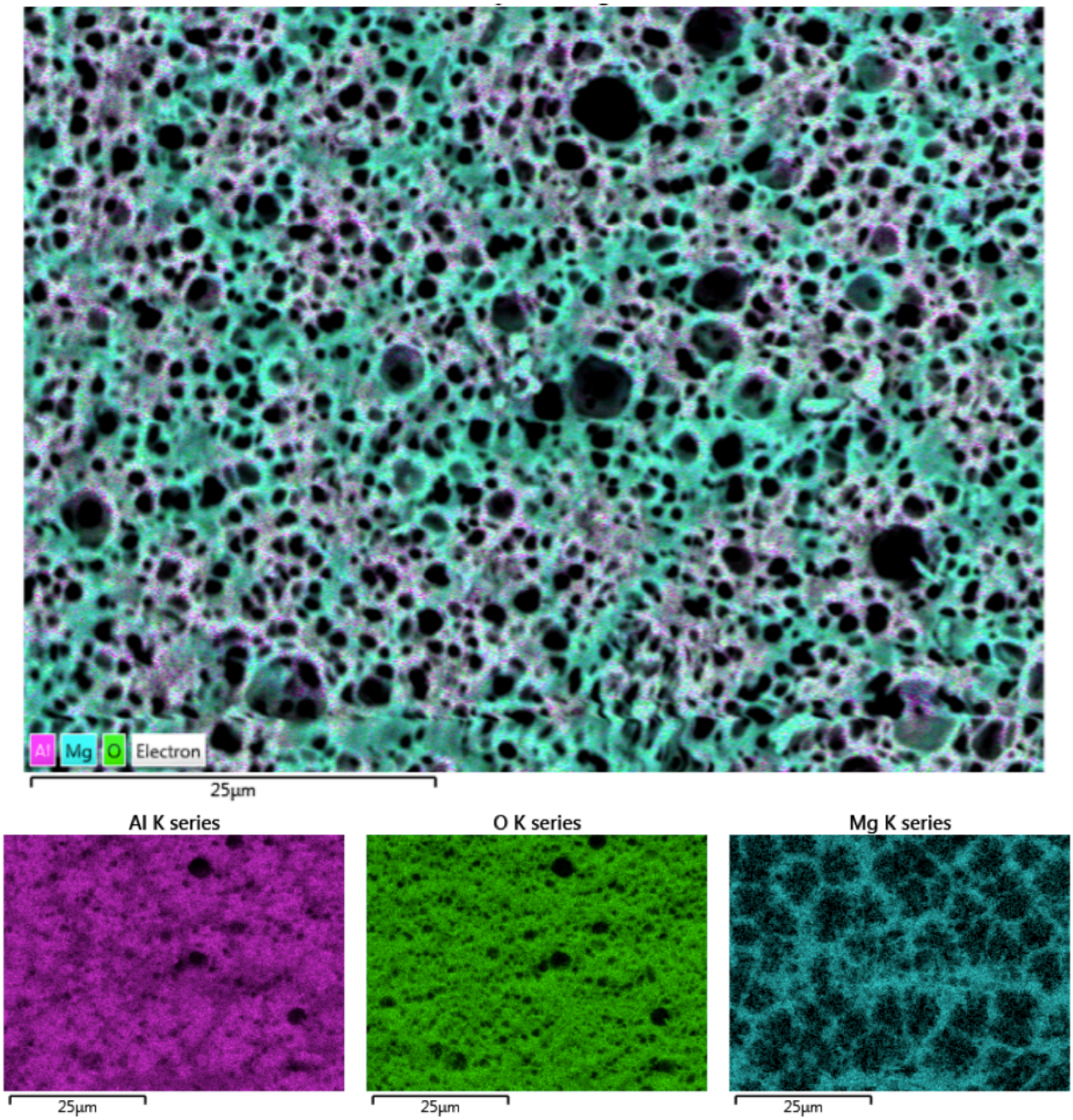

Figure 5.29: *EDS. Photo location: Approx.1/3 radius from specimen centre. Measurement scale: 25 µm. 5wt% MgO (IWI). Calcination: 1150℃.* ***Purple:*** *Aluminium, K series.* ***Green:*** *Oxygen, K series.* ***Cyan:*** *Magnesium, K series.*

From this figure it is evident that magnesium are distributed unevenly throughout the porous structure when incipient wetness impregnation is used in sample preparation. This will result in local concentration differences of magnesium. After calcination, also present phases will be locally dependent.

Sample: 1.8mm-13wt%MgO-1150

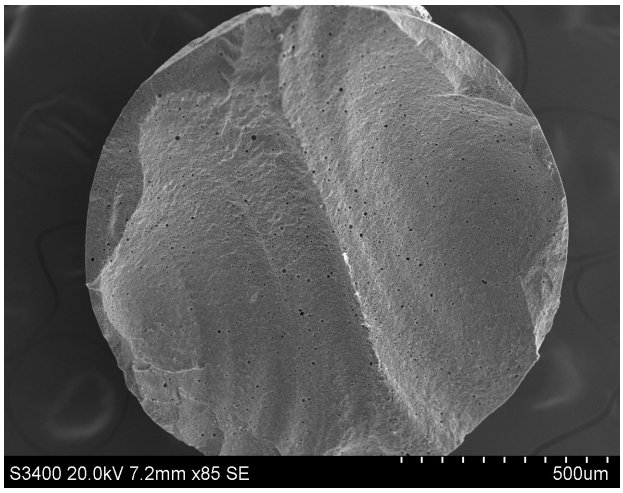

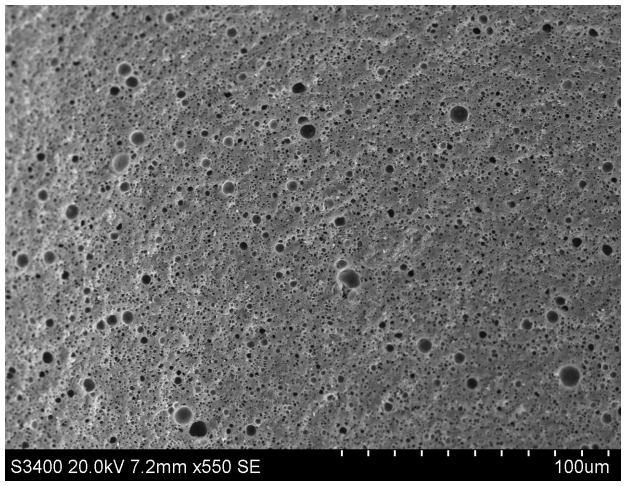

***Figure 5.30 (Left photo)**: Fracture surface. Specimen overview photo. Magnification: x 85. 13wt% MgO (IWI). Calcination temperature: 1150℃. Measurement scale: 500μm. Acceleration voltage: 20 kV.*

***Figure 5.31 (Right photo)**: Fracture surface. Specimen centre. Magnification: x 550. 13wt%-MgO (IWI). Calcination temperature: 1150℃. Measurement scale: 100μm. Acceleration voltage: 20 kV.*

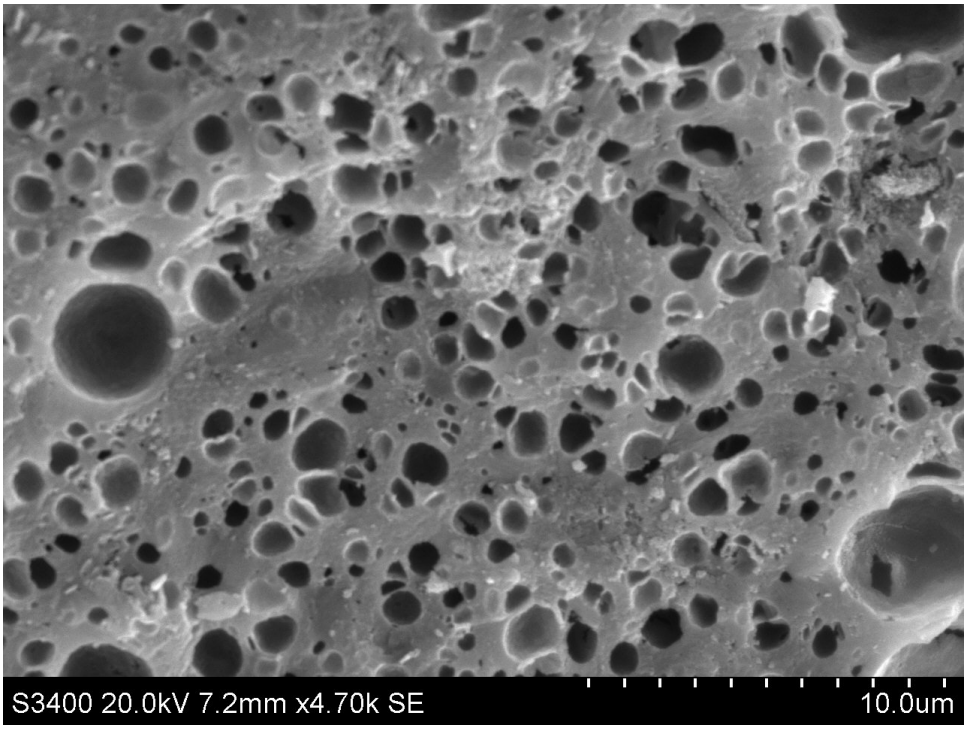

***Figure 5.32:** Fracture surface. Specimen centre. High magnification: x 4.7 k. 13wt% MgO (IWI). Calcination temperature: 1150℃. Measurement scale: 10μm. Acceleration voltage: 20 kV.*

6 Discussion

6.1 Overview

This present work has confirmed that modification of γ-alumina spheres by impregnation of magnesium salt- precursor greatly increase tensile strength and stiffness (E-modulus*) of the candidate material. A method to evaluate crush resistance of material for proppant applications was suggested. Modified alumina spheres at scope, proved more than sufficient in terms of crush resistance with respect to proppant application requirements. The clear difference in mechanical integrity between the calcined base material (α- alumina) and Mg- oxide- modified specimens proves that the formation of the spinel phase, $MgAl_2O_4$ by reaction of the Mg- oxide precursor with the γ-alumina is essential in order to increase strength at scale. In order to achieve sufficient tensile strength and crush resistance, calcination temperatures well above $\gamma \rightarrow \alpha$ transition temperature are required. Calcination temperature at 1140℃ provided highest mechanical integrity for Mg-modifyed specimens in this work.

By examining points in weibull plots where samples has a failure probability of 10%, both the reliability of the data (m- modulus), and characteristic tensile strength is combined in one integrity-describing value ($\sigma_{10\%}$). This type of evaluation is a useful tool to optimize variables such as MgO content and calcination temperature in order to obtain optimal mechanical performance.

Highest combination of weibull modulus (m), and characteristic tensile strength were observed for the 1.0 mm sized specimens, prepared with ultrasonic impregnation, containing 15wt% MgO, calcined at 1140℃. Although this sample also inhibited highest particle density, the majority of the strength increase was induced with the applied modification treatment. The highest stiffness (E-modulus*) was observed for the 1.0 mm- 12 wt.% MgO- modified sample that was prepared using (IWI) and calcined at 1150℃. This sample was accompanied by low reliability values (m), which limited its total mechanical performance. This same sample did however stand out in terms of high surface area and open pore volume recorded post high temperature calcination. XRD scans shows that broad and shifted spinel peaks were related to high BET surface area, open pore volume and along with high stiffness values. Spherical deformation (strain*) a specimen may endure before failure is also significantly increased with the modification treatments. The calculated crush resistance is about 3 times higher for ultrasonic aided Mg-oxide modified specimens, than for the commercial resin coated proppant product also tested in this work.

By applying BJH tests, pore size- distribution and average pore sizes were found to be different for 1.0 and 1.8 mm sized specimens. How this affects the distribution of metal oxide precursor within the porous alumina structure and thereby also the final microstructure is further discussed in section 6.4.

Properties required for propping agent to function efficiently and provide conductive pathways for oil and gas migration in fractures, were defined and reasoned by evaluating permeability and settling velocity equations. Most important proppant properties and can be summarized: High strength (mechanical integrity) to resist closure stress, low particle density to increase transport abilities with fluid, sphereicity and roundness for permeability, and low acid solubility for long-term integrity. The Mg- modified alumina candidate material at scope, outperforms the commercial resin- coated proppant regarding all evaluated requirements. Fines production over time and acid solubility for samples is yet unconfirmed.

For multi- functional proppant applications, additional properties are required. High degree of open porosity is needed for surfactant carrying proppants to function, and high surface area is required for catalytic proppant solutions. A significant trade-off between BET surface areas and open pore volume with increasing calcination temperature and tensile strength is observed. An increase in mechanical integrity with calcination temperature is accompanied with similar decrease in surface areas and open pore volume and vice versa. This topic is further discussed in 6.4. Figure 6.1 shows the mentioned trade-off relationship.

6.2 Weibull analysis & information

As reported in literature review, Weibull theory is based upon that when a crack first is initiated within a specimen, it immediately leads to a global failure. Random distribution of local material properties and flaws therefore governs the total strength and reliability of a structure. It follows that a specimen with homogenous properties distributed throughout its volume will display much higher reliability (m) than materials with inhomogeneous distributed properties. In weibull analysis, the homogeneity of mechanical properties distributed is directly reflected with a reliability value (Weibull modulus: m). High m- values mean high degree of homogeneity and vice versa. This trait is especially useful for evaluating materials that has been modified with impregnation of a salt precursor. In addition to evaluate pre-existing local material properties, this value (m) also provides information about how homogeneously the salt precursor was distributed in the preparation. This is among others reflected through the difference in m- value for ultrasonic and incipient wetness prepared specimens, which indicates more homogeneous MgO- distribution for ultrasonic prepared samples.

As observed in SEM photos, occasional relatively large pores, and inhomogeneous regions (Fig. 5.26) are occurs in samples. These large pores and regions are typical drivers for global failure of specimens as load is gradually inflicted. As approximated using Shipway and Hutchings relationship [25] , about 80% of total tensile stresses that occur in specimens at break, is located along the central axis between loading points. Flaws and inhomogeneous properties distributed along this central axis will thereby cause failure at lower applied load, than if flaws are located elsewhere. Considering the microstructure, γ-alumina base material consequently also has improvement potential regarding mechanical performance.

6.3 Microstructural evolution, phases and property coherence

Microstructural features accompany recorded material properties. This section will summarize most evident correlation observed.

Firstly, the significant trade-off between BET surface area and tensile strength for all samples with increasing temperature must be noted. Figure 6.1 below illustrates this correlation for 1.0 and 1.8 mm sized specimens prepared with 12- 13wt% MgO (IWI). When calcination temperature reaches 1000°C, tensile strength increases and surface area decreases rapidly for both sample sizes. However, tensile strength increase is higher simultaneously as significant surface area is kept for the 1.0- 12wt%MgO sample after 1150°C calcination. Equivalent trends are found in BJH pore volume plot (Appendix, figure 9.1).

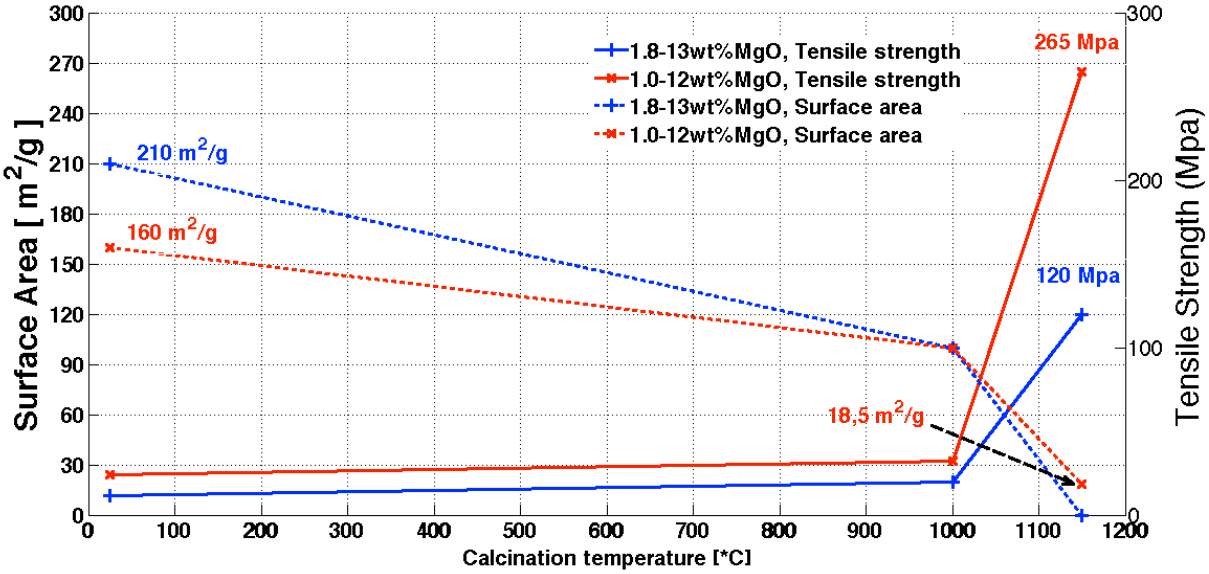

Figure 6.2: *Illustration of the trade-off that occurs between surface area and characteristic tensile strength as a function of calcination temperature for 1.0- and 1.8 mm sized spheres, containing 12-13wt%MgO.* ***Dashed lines:*** *BET surface area.* ***Whole lines:*** Weibull characteristic tensile strength

Significantly smaller $MgAl_2O_4$- spinel krystallites are approximated from XRD scans for specimen that retained BET surface area. Small $MgAl_2O_4$- spinel krystallites are also accompanied by higher degree of open porosity (figure 5.17). From a mechanical perspective; small spinel crystallites yielded higher material stiffness (E- modulus*, Figure 5.9). This is in accordance with Hall Petch relations [35].

Both $MgAl_2O_4$- spinel and α- alumina crystallites generally increase in size with increasing calsination temperatue. Ultrasonic prepared samples stands out in this contex where larger crystallites are observed after lower calcination temperature. This observation contributes to support the argument that ultrasonic impregnation leads to greater final dispersion of MgO. (Further evaluated in 6.4.)

M. Rotan [6], concluded that increase in mechanical properties was related to strong intergranular bonds that formed between the small spinel crystallites and α-alumina phase. He also proposed that high temperature calcination would coarsen of spinel crystallites that enlarge the contact area between the adjacent crystallites, forming a rigid network that leads to increased mechanical properties. On this basis, there must also exist a peak in mechanical properties where crystallites are coarse enough to reach the point of optimal contact area between adjacent crystallites, but still not too coarse so that the Hall Petch effect weakens the material. This mechanical "performance-peak" could be found with Weibull analysis of compression data as a useful tool. The point where both weibull modulus and characteristic strength reaches a peak might thereby correspond to the optimal microstructure for mechanical performance for materials prepared with impregnation.

High mechanical performance is however not followed by high surface area and open pore volume as clearly demonstrated in this work. But as mentioned, high surface area was in coherence with small crystallites, which again were observed in samples with very high stiffness (E-modulus*) but low (m). This proposes that stiffness measurements might indicate retained surface area and open pore volume. This correlation also suggests that even better combinations of mechanical performance and high surface area are achievable if weibull modulus were improved with more homogeneous distribution of MgO at right concentrations.

6.4 Distribution of impregnated magnesium oxide precursor

M.Rotan[6], pointed out that distribution of impregnated salt in γ- alumina aggregates is first of all dependent of the microstructure of the porous support. A homogeneous distribution of primary γ- alumina crystallites in aggregates is desirable to enable the impregnated solution to access the entire volume of the aggregate. Rotan showed with element mapping that significant variation in Ni- concentrations throughout the aggregate was accompanied with packing density variations of γ- alumina crystallites. High packing density of crystallites prevented distribution of salt precursor, yielding areas with low NiO- content.

Large local variation in MgO- concentrations tough out the porous aggregate is also demonstrated with EDS mapping in this work (Figure 5.29). Magnesium- oxide concentration variations will affect the microstructure of the end product post calcination.

XRD scans (Fig. 5.18 & 5.20) proves significant differences between the 1.8 and 1.0 mm sized samples regarding final crystallite structure. This result was unexpected considering equal preparation method and similar nominal MgO- contents. Since also the calcined base material (α-alumina) for the two samples displayed the exact same XRD "fingerprints" (figure 5.18), the final difference found in modified samples cannot originate form crystallite differences in base materials.

Average pore diameter and pore size- distribution are displayed in figure 5.13 & 5.14 for. Figures show smaller average pore diameter and broader pore size distribution for 1.8 mm spheres than for 1.0 mm spheres (γ-alumina). Avereage pore diameter is approx. 10.5 nm for 1.8- specimens, and 12.5 nm for 1.0- specimens.

As it appears, average pore sizes and distribution governs the distribution of salt precursor, the dispersion of MgO after drying, and the final microstructure after calcination. Arguments below will support this claim.

Firstly, lets consider the geometrical relations of a sphere. The sphere represents a pore in this occasion. While volume of a sphere is proportional to r^3, the surface area that represents the inner surface of the pores in this occasion, is proportional with r^2. As the pore radius increase, the pore volume that could be filled with a liquid salt precursor will increase at rates faster than for the inner surface of the pore. This can be illustrated with an example using the average pore sizes obtained form the two different spheres under investigation. When pore diameter increases from 10.5 nm to 12.5 nm, the inner surface area will increase with approx. 41% while pore volume will increase with about 68%. This will result in more volume of liquid salt precursor available to be deposited on a relatively smaller inner surface area for larger pores, after drying. Higher local concentrations of metal oxide are therefore found in impregnated supports with larger average pore diameters. Low weibull moduli recorded for the sample with larger pore diameter and thereby also larger differences in local MgO- concentrations support this suggestion.

Secondly, it is reasonable to consider the capillary forces in this context, which are pulling liquid salt precursor into pores in incipient wetness impregnation (IWI). The equation determining the height of a meniscus:

$$h = \frac{(2*\gamma*Cos(\theta))}{\rho*g*r} \quad (6.1)$$

***Equation 6.1**: Height of a meniscus*

Equation 6.1 is only provided to illustrate a point, and does not directly apply for the investigated porous material. The height of a liquid with density ρ, in a vertical pipe with radius r, is given. Rest of the variables may be considered constants for this argument. The thinner the tube gets (smaller radius), the higher the fluid will travel in the vertical tube. Also dens fluids will travel shorter than thinner solutions.

If similar correlation also applies for liquid salt precursors traveling into porous alumina support, smaller average pore sizes will yield more homogeneous distribution of precursor and denser precursor solutions would slow distribution and cause larger local differences in metal oxide concentrations.

Figure 6.2 present changes in weibull modulus as a function of wt.% MgO for samples calcined at 1150℃ and prepared with IWI. A linear decline in weibull modulus with increasing MgO content is found for the 1.8 mm spheres. A peak in weibull modulus is observed at 5wt% MgO content for the 1.0 mm spheres.

Observations in figure 6.2 are gently supported by arguments associated with equation 6.1. Precursors mixed with high Mg-nitrate concentrations will become more dens that will slow down distribution with capillary forces. The resulting high local MgO- concentrations then reduce m-values. Small average pore sizes as observed for 1.8 size spheres, will provide better distribution of densely mixed precursors that will be reflected in higher weibull modulus.

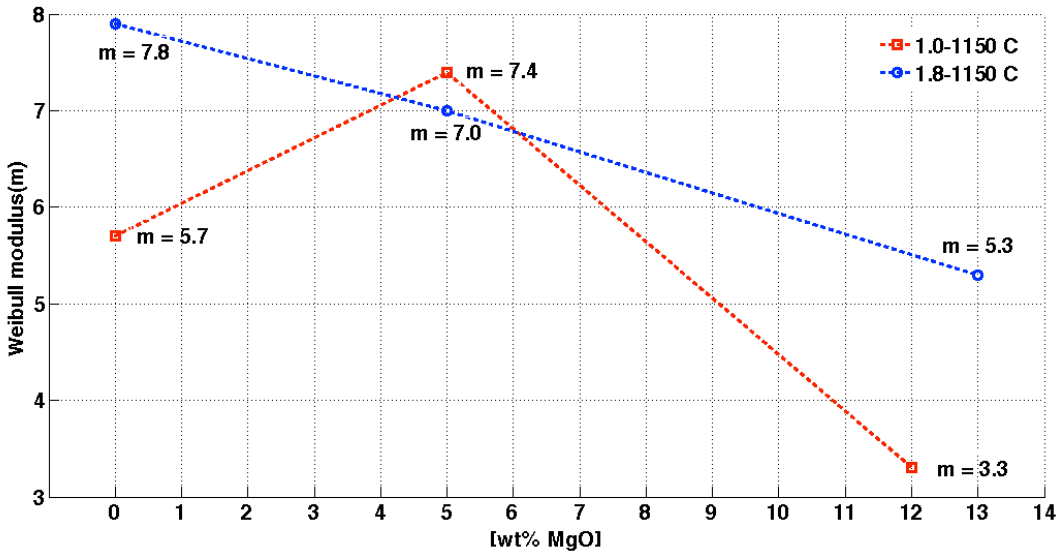

Figure 6.2: *Weibull modulus as a function of wt.% MgO content for 1.0 and 1.8 mm sized spheres at fixed calcination temperature (1150 ℃). Samples were prepared with IWI.*

Samples prepared with ultrasonic impregnation and 15wt% MgO are not included in this figure, but inhibits higher weibull modulus than the 12wt% MgO, incipient wetness- impregnated sample (table 5.4). This may indicate greater dispersion of MgO for ultrasonic prepared samples.

6.5 Multi functional proppants

The modified candidate material meets or exceeds requirements for proppant application both in terms of permeability related geometrical properties and material strength. With respect to crush resistance, all modified 1.0- samples calcined above 1140℃, significantly outperformed the resin coated proppant product tested. The ultrasonic modified sample, with its crush resistance calculated to 30 000 PSI, meets requirements for extreme high closure- stress reservoirs. However, more extensive testing with ISO-13503-5 [15] are needed to confirm long term permeability of specimens. Acid solubility tests and crushing tests also form ISO-13503-2 [14] needs to be carried out to fully qualify the modified candidate material as a propping agent.

Comparison of calculated crush resistance from this work with the crush resistance test in ISO-13502-3 should be carried out in order to test the accuracy of the calculation.

For multi functional proppant application, 1.0-12wt%MgO-modified sample calcined at 1150℃, showed most promising features. Still after high temperature calsination, significant amounts of open porosity and surface area were retained. With its crush resistance calculated to 14000 PSI (97 MPa), this solution is suitable for high closure stress reservoir fractures. BET surface area is 18.5 m^2/g. Subsequent experiments carried out with ultrasonic samples proved that calcination temperature of 1140℃ is more favourable, both in terms of strength and surface area. On this basis it is reasonable to assume that also the 1.0-12wt%MgO- modified sample would have inhibited increased surface area if it was calcined at 1140℃ instead of 1150℃.

In addition to high surface area propping agent, high temperature is needed in reservoir environment for catalytic reactions to take place. In some rare extreme high temperature wells, the thermometer may reach 260°C [8]. If this temperature is sufficient to activate and drive desired catalytic reactions are not investigated. High temperature wells also inhibit high closure stresses, and proppants would needs to withstand up to 30 000 PSI. To obtain strength values sufficient to handle 30 000 PSI closure stresses in combination with high surface area could become challenging with the selected candidate material.

For now, the surfactant carrying proppants solution seems more promising. Best combination solution was crush resistance of 14000 PSI with a total of approx. 20% open porosity. In other words, 20% of the total volume of proppants applied can be impregnated with a friction reducing surfactant and placed in a high-pressure fracture. If productivity benefits of surfactant carrying proppants surpasses benefits related to resin coated products, can be investigated by comparing different products with the long-term permeability test described in ISO-13503-5 [15].

7 Outlook

Based on present investigation, first priority in further work should be dedicated to find the calcination temperature where optimal mechanical properties occur for the candidate material. Results show that lowering calcination temperature form 1150°C to 1140°C for ultrasonic prepared samples increases mechanical properties. Based on this and other results, it is suggested that the optimal calcination temperature should occur in the region between 1125°C and 1145°C. Optimal calcination temperature can be located by making one large batch with incipient wetness impregnation to ensure equal impregnation treatment, and divide this batch into 5-10 smaller samples after drying. These samples should further be calcined in the temperature region mentioned above, before uniaxial compression and weibull analysis of specimens are carried out. Investigating tensile strength values where failure probability is 10% should provide a good basis for comparison of mechanical properties when both characteristic strength and reliability is considered with this measure.

Secondly, focus should be shifted to encapsulate the optimal MgO- content to obtain high surface area and open porosity. As reported in this work, local MgO –concentrations are varying throughout the bulk phase of the modified materials and are most likely dependent on pore diameter and pore size distribution of the support base (γ- alumina). Also the impregnation method applied affects the final distribution of MgO in the microstructure. Because of these variables, it is suggested to only experiment with one base material product is carried out to make the process less complicated. Broad XRD peaks for $MgAl_2O_4$-spinel phases were accompanied by higher surface area after high temperature calcinations. This sample also inhibited low weibull modulus values that imply large local differences in MgO- distribution and local concentrations above the 12wt% MgO- nominal concentration impregnated. Of that reason nominal impregnations concentrations above 12wt% MgO is suggested for incipient wetness impregnation of 1.0 Sasol alumina spheres.

When broad XRD peaks and small $MgAl_2O_4$-spinel are obtained resulting in high surface area, element mapping with EDS or WDS can be used on fracture surfaces to find local MgO-concentrations that actually causes these broad XRD peaks. Generally more SEM investigations can be performed to confirm/debunk correlations.

Being desirable to obtain high surface area, and open pore volumes this local MgO –concentration found in element- mapping, may represent a new standard for MgO concentration- level. Next step to achieve further improvement is then to investigate various impregnation methods for more homogeneously distribution of metal oxide throughout the bulk volume. Ultrasonic aided impregnation was found to increase weibull modulus and tensile strength for samples compared with incipient wetness impregnation. This indicates that more homogeneous distribution of metal oxide was obtained with ultrasonic impregnation. Sharper XRD peaks for ultrasonic also support this argument.

Impregnation may be carried out in several steps with drying in-between to obtain desired local and global metal oxide concentrations. As a more innovative experimental suggestion: Different ultrasonic wavelengths might aid in impregnating different pore sizes enabling more homogeneous concentration distribution.

Based on present findings it is also suggested that impregnation treatments of support materials should be adjusted for pore diameters and distribution inhibited of the material at hand, and not only depend on total water- absorption. like today. A standard procedure for this can be created when better understanding of correlations and more solid proofs are obtained.

As for the proppant part, the mentioned ISO- tests represent a basis for qualification and comparison of products. An ISO13503-2 crush test should be first priority of check accuracy for the crush resistance approximations for in this work.

8 Conclusion

In present work the effect of modification treatments on alumina-based supports has been investigated, focusing on the potential usage of the candidate material for multi- functional proppant applications in unconventional oil and gas reservoirs. Motivations include enabling higher production efficiency by upgrading hydrocarbons in- situ with catalytic proppants, or reduce friction in wells with surfactant carrying proppants. Today, proppants are only applied to provide permeable pathway for oil and gas migration by resisting closure stress in fractures.

The objectives of this work were to define material properties requirements for proppants and for multi-functional proppant solutions, prepare the candidate material before investigating the impact modification treatments inflicted with respect to the defined requirements. Most important requirements for proppants and multifunctional proppants can be summarizes as: Low particle density, high crush resistance, spheres and roundness, narrow size distribution of particles, high surface area and high degree of open porosity.

With uniaxial compression of specimens and Weibull strength analysis it was proved that impregnation of a liquid MgO- precursor into alumina-based supports with subsequent calcination, significantly improve mechanical performance of the material. An unknown fraction of the strength increase is however due to densification of material inflicted by calcination. By using weibull plots and random packing factors of spheres, crush resistance for the candidate materials were approximated.

Highest mechanical performance was obtained for samples prepared with ultrasonic impregnation with subsequent calcination at 1140℃. Crush resistance for this sample were approximated to 30000 PSI, outperforming the commercial resin coated proppant with a factor of three. Increased mechanical performances for ultrasonic prepared specimens compared to incipient wetness impregnated specimens are most likely due improved distribution of liquid salt precursor during impregnation. XRD scans, and differences in weibull modulus support this claim. Strength increase of materials seems to be a function of precursor distribution and impregnation method rather nominal metal oxide concentration. To obtain surface area and open pore volume, metal oxide concentration is more essential. This claim is supported by the fact that all samples impregnated with an arbitrary MgO concentration had significant strength increase and similar XRD fingerprints, whereas surface area and open pore volume only were found for one specific MgO- concentration.

A clear trade-off between surface area, open pore volume and tensile strength with increasing calcination temperature is evident. Decline in surface area and increase in tensile strength are inversely proportional and changes most rapidly when calcination enters $\gamma \rightarrow \alpha$ trasition temperatures. One sample did retain surface area and open pore volume in combination of high tensile strength after modification treatment and high temperature calcination. This confirms the possibility and potential of creating multi- functional proppant solutions based on MgO- modified aluminas.

Differences found in XRD scans, weibull analysis and in pore diameters between 1.8 and 1.0 mm sized specimens after similar modification treatments indicate that distribution of metal oxide precursor is dependent on average pore diameters and pore size distribution in addition to water absorption. Of that reason, it is suggested that also impregnation procedure of porous support materials are adjusted for different pore sizes -and distributions.

This work also presents some of the benefits of applying Weibull analysis in evaluation of mechanical properties of metal oxide -modified aluminas.

Porous high- strength and surface area materials as investigated, is also useful in other applications such as membranes or catalysts. Results obtained in this work, imply that further improvement of combined properties for the candidate material is within reach.

.

9 Appendix

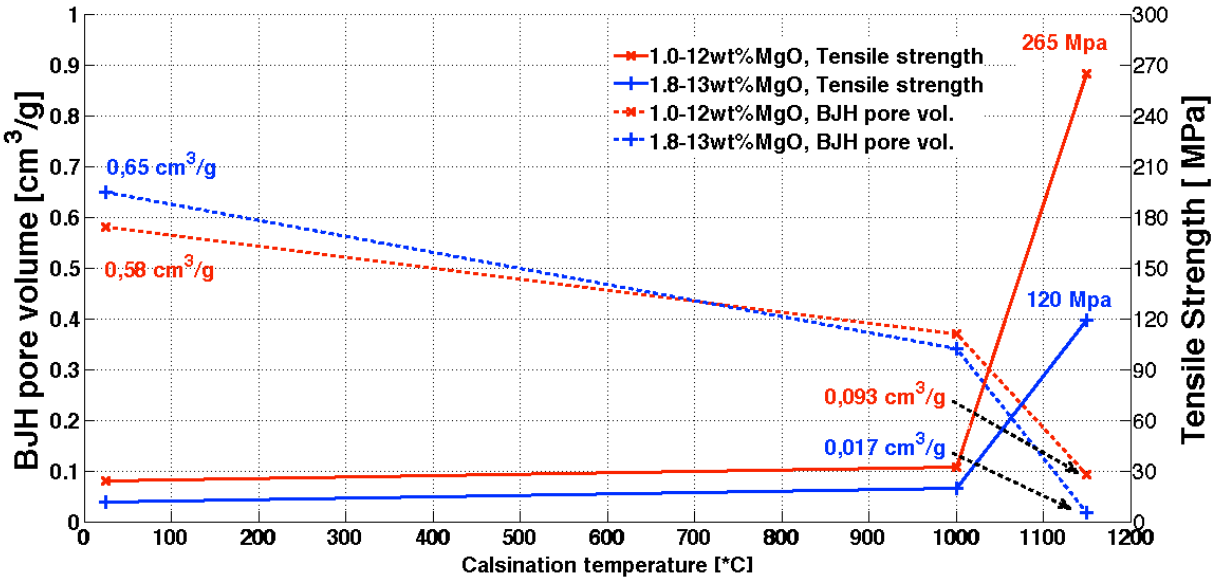

Figure 9.1: *Illustration of the BJH pore volume and characteristic tensile strength trade-off.*

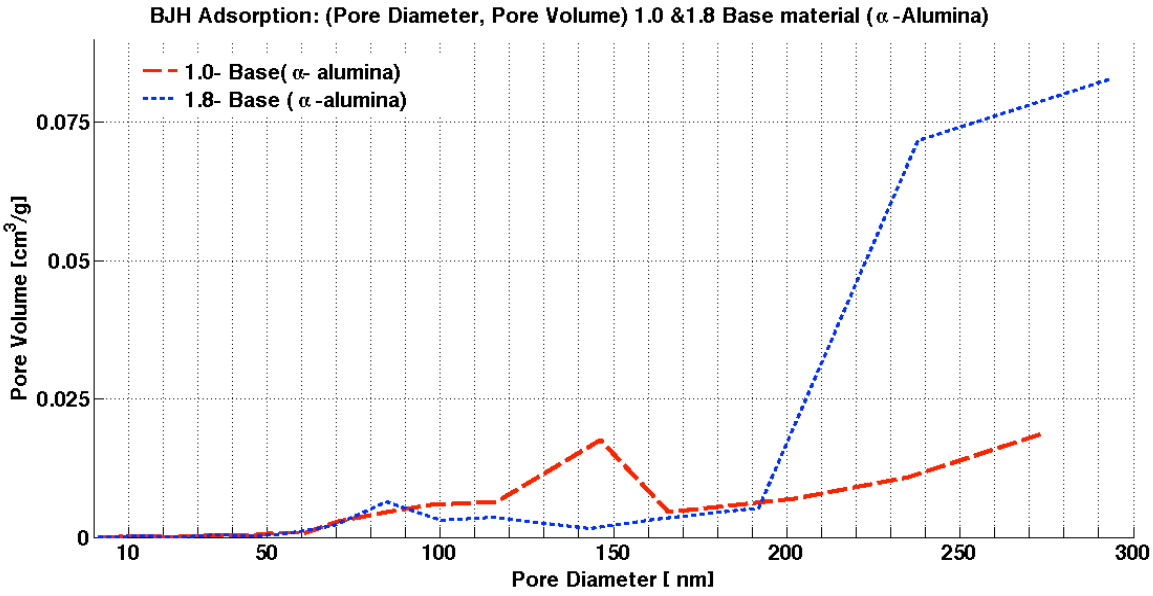

Figure 9.2: *Pore volume distributed over pore diameters for α-alumina samples. (Calcination 1150°C)*

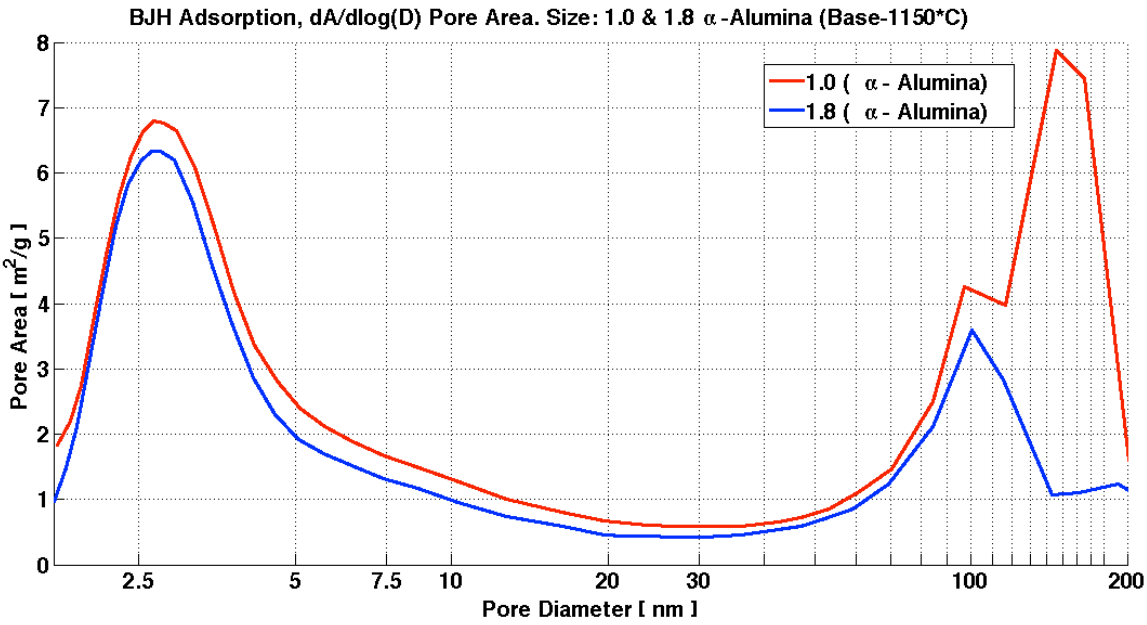

Figure 9.3: *Pore area distributed over pore diameters for α-alumina samples. (Calcination 1150℃)*

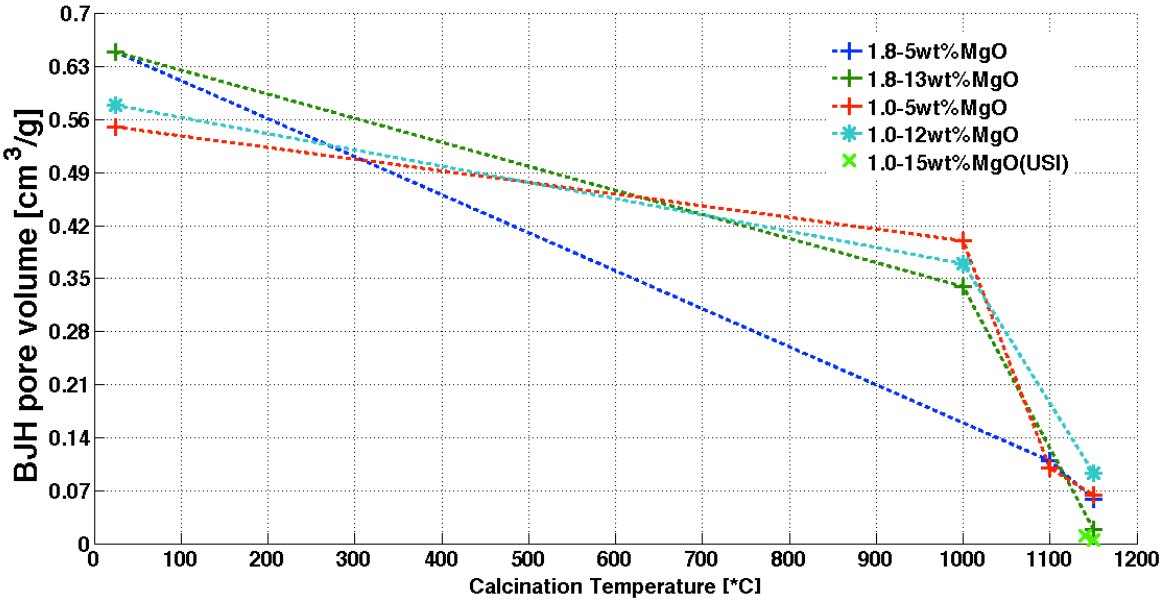

Figure 9.4: *BJH pore volume as a function of calcination temperature for 1.0 and 1.0 mm sized samples prepared with 5, 12,13 and 15 wt%MgO. Impregnation: IWI &USI (light green cross).*

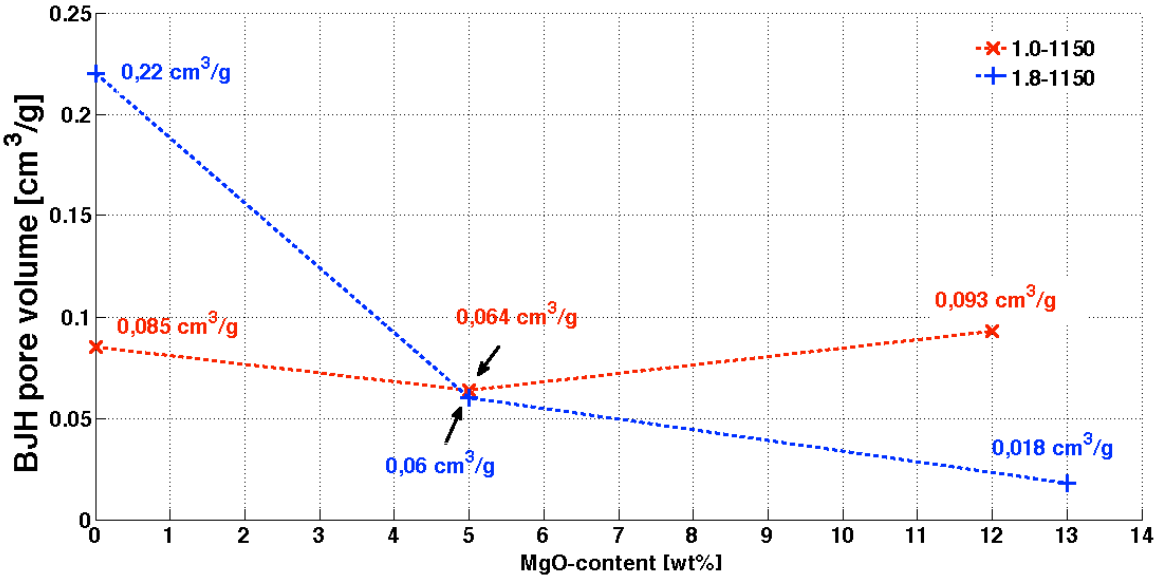

Figure 9.5: *BJH Pore volume as a function of wt.% MgO for sphere size 1.0 &1.8 mm at fixed calcination temperature 1150*℃.

10 References

1. Petroleum, B. *Energy Outlook 2030*. 2013; Available from: http://www.bp.com/content/dam/bp/pdf/statistical-review/EnergyOutlook2030/BP_Energy_Outlook_2030_Booklet_2013.pdf.
2. report, P.I.G. *Shale gas should replace EU coal-fired power* 2012; Available from: http://pipelineandgasjournal.com/shale-gas-should-replace-eu-coal-fired-power-uk-economist.
3. John R. Hellmann, B.E.S., Walther G. Lushcer et al., *Proppants for shale gas and oil recovery.* American Ceramic Society Bulletin, 2013. **93**(1).
4. Ottestad, E., *Proppants, properties and Requirement*. 2013, NTNU.
5. Wikipedia. *EOR*. Available from: http://en.wikipedia.org/wiki/Enhanced_oil_recovery.
6. Rotan, M., *Phase composition, microstructure and resistance to attrition of alumina- based support for Fischer- Tropsch catalyst*. 2012, NTNU Norwegian University of Science and Technology.
7. Don, L., *Proppants open production Pathways.* 2011.
8. Schlumberger. *High pressure, High temperature (HPHT)*. 2014; Available from: http://www.slb.com/services/technical_challenges/high_pressure_high_temperature.aspx.
9. King, G.E. *Fracturing Basics*. 2009; Available from: http://gekengineering.com/Downloads/Free_Downloads/Fracturing.pdf.
10. *Determining the Settling Velocity*. Available from: http://www.rpi.edu/dept/chem-eng/Biotech-Environ/SEDIMENT/sedsettle.html.
11. T.T Palisch, S., CARBO Ceramics; M.C Vincent, SPE, *Slickwater Fracturing Food for Thought.* 2008.
12. Software, M.F. *Calculated fracture permeability*. Available from: https://downloads.mfrac.com/Meyer-2012/manual/en/mfrac.04.09.html.
13. C. Mark Pearson, S.C.C.I., *Dimentionless fracture Conductivity: Better Input Values Makes Better Wells.* 2001.
14. Standardization, I.O.f., *ISO 13503-2 Recommended Practice for Measurement of Properties of Proppants Used in Hydraulic fracturing and gravel- packing Operations*.
15. Standardization, I.O.f., *ISO 13503-5; Procedures for measuring the long-term conductivity of proppants*.
16. Jirasek, M., *Size effect on structural strength (civil engineering)*. 2006, McGraw-Hill Education: http://www.accessscience.com.
17. Wikipedia. *Size effect on structural strength*
18. C. Subero-Couroyer, M.G., N. Brunad and F.Kolenda, *Weibull analysis of quasi-static crushing strength of catalyst particles.* 2003.

19. Richerson, D.W., *Modern ceramic engineering: properties, processing, and use in design*. Vol. 29. 2006: CRC press.
20. Kováčik, J., *Correlation between Young's modulus and porosity in porous materials.* Journal of materials science letters, 1999. **18**(13): p. 1007-1010.
21. Asmani, M., et al., *Influence of porosity on Young's modulus and Poisson's ratio in alumina ceramics.* Journal of the European ceramic society, 2001. **21**(8): p. 1081-1086.
22. Oka, Y.H.a.Y., *Determination of the tensile strength of rock by a compression test of an irregular test piece.* International Journal of Rock Mechanisems and Mining Science, 1966.
23. Y. Li, D.W., J. Zhang. L. Chang, Z. Fang, Y. Shi, *Measurements and statics of single pellet mechanical strength of differently shaped catalysts.* 2000.
24. Kschinka, B.A. and S. Perrella, *Strengths of glass spheres in compression.* Journal of the American Ceramic Society, 1986. **69**(6): p. 467-472.
25. Shipway, P.H. and I.M. Hutchings, *Fracture of brittle spheres under compression and impact loading. I. Elastic stress distributions.* Philosophical Magazine A, 1993. **67**(6): p. 1389-1404.
26. Shipway, P.H. and I.M. Hutchings, *Attrition of brittle spheres by fracture under compression and impact loading.* Powder technology, 1993. **76**(1): p. 23-30.
27. WR. Dean, I.M.S., H.W Parson, *Distribution of stress in a deccelarating elastic sphere*. 1952. p. 212-234.
28. Bernhardt, M., *Development of high performance lightweight aggregates*. 2013, NTNU- Norwegian University of Science and Technology: Trondheim, Norway.
29. Wen, Z., L.I.N. Ling, and Z. Chongyu, *<FONT face=Verdana>Preparation of supported nickel™≤basd catalyst by ultrasonic impregnation method and its catalytic performance</FONT>.* Industrial Catalysis, 2011. **19**(5): p. 26-${article.jieShuYe}.
30. Zhang, Y., et al., *Novel ultrasonic-modified MnOx/TiO2 for low-temperature selective catalytic reduction (SCR) of NO with ammonia.* J Colloid Interface Sci, 2011. **361**(1): p. 212-8.
31. Division, S.I. *Shaped Carriers Produced from High Purity Aluminas, Silica Aluminas and Hydrotalcites*. Available from: http://www.sasolgermany.de/fileadmin/doc/alumina/Sasol_Spheres_and_Extrudates-Dec2009_web.pdf.
32. Bartholomew, C.H. and R.J. Farrauto, *Fundamentals of industrial catalytic processes*. 2011: John Wiley & Sons.

33. Wikipedia. *Weibull*. Available from: http://en.wikipedia.org/wiki/Weibull_distribution.
34. Petrovic, J.J., *Weibull statistical fracture theory for the fracture of ceramics.* Metallurgical Transactions A, 1987. **18**(11): p. 1829-1834.
35. Hansen, N., *Hall–Petch relation and boundary strengthening.* Scripta Materialia, 2004. **51**(8): p. 801-806.